Journal of Peridynamics and Nonlocal Modeling manuscript No.
(will be inserted by the editor)

Huy Anh Nguyen · Hanlin Wang · Satoyuki Tanaka ·
Selda Oterkus · Erkan Oterkus

An In-depth Investigation of Bimaterial Interface Modeling Using Ordinary State-based Peridynamics

Received: date / Accepted: date

Abstract This study presents an in-depth investigation of interface modeling techniques in ordinary state-based peridynamics (OSB-PD). By performing numerical examples, the accuracy of each technique is investigated by comparison with the finite element solutions for simple bimaterial interface problems. Subsequently, the capabilities of OSB-PD in treating material interfaces with complicated geometries are demonstrated by solving various problems with a single inclusion or multiple inclusions. Finally, a cracked plate containing an inclusion is considered to study effects of the inclusion on dynamic stress intensity factor (DSIF). The OSB-PD shows its huge potential in modeling a structure with multiple defects due to the effectiveness and ease of implementation.

Keywords Peridynamics · Material interfaces · Peridynamic differential operator · Inclusions

1 Introduction

The modeling of defects such as voids, inclusions, or cracks is of paramount importance in engineering analysis because the existence of such defects strongly affects the structural integrity and performance. Additionally, the accurate modeling can improve the prediction of mechanical behaviour and macroscopic material properties. Hence, this problem has attracted great attention of researchers and practitioners to enhance the accuracy and effectiveness of numerical methods to better represent the defects in structures.

The conventional finite element method (FEM) is arguably one of the most popular techniques being used to solve a wide range of engineering problems due to its capabilities to produce highly accurate

---

Huy Anh Nguyen
Graduate School of Advanced Science and Engineering, Hiroshima University, Higashi-Hiroshima, Japan
E-mail: anhhuy.nguyen.vnn@gmail.com

Hanlin Wang
Graduate School of Advanced Science and Engineering, Hiroshima University, Higashi-Hiroshima, Japan
E-mail: hanlin_wang_2013@163.com

Satoyuki Tanaka
Graduate School of Advanced Science and Engineering, Hiroshima University, Higashi-Hiroshima, Japan
E-mail: satoyuki@hiroshima-u.ac.jp

Selda Oterkus
Department of Naval Architecture, Ocean and Marine Engineering, University of Strathclyde, Glasgow, United Kingdom
E-mail: selda.oterkus@strath.ac.uk

Erkan Oterkus
Department of Naval Architecture, Ocean and Marine Engineering, University of Strathclyde, Glasgow, United Kingdom
E-mail: erkan.oterkus@strath.ac.uk

solutions and handle complex geometries. In order to model defects, however, FEM requires element boundaries conform to material interface and cracks, so it results in an increase in mesh generation time to achieve satisfying meshes. Furthermore, mesh refinement is needed in the vicinity of cracks or material interfaces owing to the presence of high displacement gradients at these locations. Consequently, not only does the construction of conforming meshes become more time-consuming, but the amount of computational time also significantly rises. Over the past decades, there are various methods that have been proposed to mitigate the drawbacks of FEM in solving the class of problems related to material interfaces. Unlike the traditional FEM, which employs triangle and quadrilateral elements for approximating geometries, polygonal FEM utilizes polygonal elements, hence offering greater flexibility in meshing arbitrary and complex geometries. The polygonal FEM has been extensively used to resolve many engineering applications including contact-impact [1], fracture mechanics [2, 3], large deformation [4, 5], and it was also employed in the analysis of the weak discontinuity problems. For tackling arbitrary interfaces in the polygonal FEM, Khoei and Biabanaki [6] introduced an approach in which a uniform non-conformal mesh is decomposed into polygonal elements conforming to the internal interfaces and arbitrary geometries using the concept of conformal decomposition FEM and the level set method. Ding et al. [7] presented a fast and efficient adaptive polygonal FEM based on the cut-cell method and quadtree refinement for modeling holes and inclusions. Nevertheless, in these approaches, a conformal mesh remains essential to capture the discontinuity in the models.

To completely remove the need for a conforming mesh to physical surfaces, Belytschko and Black [8] firstly proposed the extended FEM (XFEM) to model issues pertaining to strong discontinuity in which cracks and crack growth are allowed to cut through elements. Subsequently, Sukumar et al. [9] extended its applications to model arbitrary holes and inclusions without meshing the internal boundaries by the implementation of the level sets. The underlying idea of this technique is to enrich the FE approximation space by adding local enrichment functions around the discontinuities under the concept of partition of unity (PU) [10]. Basically, the enrichment functions can be chosen based on a priori knowledge about the behaviour of the solution field so that they can improve accuracy of the approximation around discontinuities. For instance, in fracture mechanics analysis, it is well-known that the singular behaviour is observed near the crack tip, so the enrichment can be defined to directly incorporate this knowledge to the FE approximation space. In order to model cracks in XFEM, two types of enrichment functions are commonly used: a Heaviside function to describe the jump in displacement field across the cracks and a set of the near-tip asymptotic fields to capture the singularity of stresses near the crack tip [11]. With the application of local enrichment functions coupled with the PU property, a crack is not necessary to be aligned with the element edges, so the mesh is independent of the geometries of discontinuities. After the first introduction by Belytschko, XFEM is becoming a popular and powerful tool to model weak and strong discontinuous problems [12–16]. Furthermore, PU and enrichment concepts are also employed to handle discontinuous problems in other methods such as finite cell theory [17], extended isogeometric analysis (XIGA) [18, 19].

As an alternative to the mesh-based methods, meshless method such as element-free Galerkin method (EFGM) [20] is known to be more suitable for modeling large deformation and crack propagation problems. With regard to material inhomogeneities, there are several works carried out to improve the accuracy of modeling discontinuous derivatives in meshless methods. Cordes and Moran [21] developed a technique in which an inhomogeneous body is considered as separate homogeneous bodies, and the interface conditions are enforced by introducing additional constraints at the variational level using the Lagrange multipliers. As a result, this approach introduces more additional unknowns, and interface nodes have to be added along the interface. Krongauz and Belytschko [22] modeled the material interface by adding special jump functions containing discontinuities in derivatives into the standard EFGM shape functions to enrich the approximation. Although the method demonstrates good accuracy and avoids oscillations at the surface of discontinuity as compared to conventional meshless approximations, additional unknowns are also required to represent the strength of the discontinuity, and it is tedious to extend this method to complex interfaces or 3D applications. Several improvements in the special jump function have been made by Wang et al. [23], Masuda and Noguchi [24]. A discontinuous Galerkin meshfree formulation was proposed to treat the material interface in composite solids by Wang et al. [25]. In this method, the problem domain is decomposed into patches associated with their material properties, and they are combined together. The jump in displacement gradient across the material interface is modeled by the boundary of the adjacent patches, and the continuities of displacement and traction are weakly enforced in the variational form, so no additional unknowns like Lagrange multipliers or special jump functions are required. Recently, Wu et al. [26] developed a novel immersed meshfree Galerkin method to model composite solids. Since this approach employs the overlapping meshes, the base material and inclusions can be discretized independently of each other. Consequently, the mesh of the base material is not necessary to conform to the material interface. In addition to weak discontinuity, the meshfree method has been successfully used to deal with fracture problems [27–29].

Despite the fact that there has been a rapid progress on numerical methods to address challenges posed by cracks and material interfaces, there remain major limitations for traditional methods to solve these problems. For example, when it comes to modeling multiple interfaces, the complexity of treatment can greatly increase in terms of mathematics and programming. Additionally, the difficulties are more obvious when the presence of material and displacement discontinuities are in the same model. In these cases, the accurate representation of defects itself is a serious challenge, let alone model the evolution of cracks. The main reason of the aforementioned difficulties lies in the fact that the traditional methods, e.g., FEM and EFGM, are based on the classical continuum mechanics (CCM) whose governing equations contain spatial partial derivatives, and these spatial derivatives are invalid at discontinuities, e.g., cracks or interfaces. Therefore, traditional methods suffer from inherent limitations with the presence of discontinuities.

In order to overcome such limitations, Silling [30] introduced peridynamic (PD) theory as an alternative to the CCM. In PD theory, the governing equation is an integro-differential equation, and it is free of spatial derivatives of the displacement field. Thus, the PD equations are valid everywhere regardless of discontinuities, and it is appropriate for problems involving cracks or interfaces. The original form of PD, namely bond-based PD (BB-PD), assumes that a material point interacts with its family of neighbouring points through pairwise interactions called bonds, and the deformation of a bond is independent of other bonds. However, the independence of pairwise interactions results in a constraint in material properties, which is the Poisson's ratio is required to be $1/3$ for 2D plane stress and $1/4$ for plane strain and 3D problems. Furthermore, it is unable to separate a deformation state into volumetric and deviatoric parts, so it is generally difficult to develop advanced material models in BB-PD. To get around these limitations, Silling et al. [31] proposed the state-based PD (SB-PD), in which the deformation of a bond is influenced by the collective deformation of other bonds, and the volumetric and distortional deformations can be separated. The SB-PD can be classified into ordinary state-based PD (OSB-PD) and non-ordinary state-based PD (NOSB-PD). While a force state vector of a bond is required to be parallel to the deformed configuration of that bond in OSB-PD, this requirement is unnecessary in NOSB-PD. The SB-PD has been employed to build various advanced constitutive models, e.g., plasticity [32, 33] and hyperelasticity [34].

In recent years, there is a rapid growth in applying PD to resolve discontinuous problems [35–39]. However, the range of PD applications is not limited to fracture, but it has been extended for the analysis of beams and shells [40, 41], heat transfer [42, 43]. An extensive review of the current PD theory and its applications can be found in [44, 45]. Additionally, different nonlocal theories have been proposed to facilitate converting the local differential operators into theirs nonlocal forms such as nonlocal operator method [46], PD differential operator (PDDO) [47]. Since PDDO employs the concept of PD interactions, it has many characteristics in common with PD. Moreover, PDDO offers a robust approach to accurately determine the derivatives of a function without explicitly performing the differentiation, and the implementation of PDDO, especially in the computation of derivatives, is quite simple as compared to other methods such as reproducing kernel particle method and moving least square, all of which basically require the explicit differentiation to obtain the derivatives of a function. Therefore, PDDO is adopted to calculate the gradient of displacement field in this study.

Although the number of works on PD is significantly increasing lately, there are a relatively small number of papers available in the literature addressing material interface modeling. Kilic and Madenci [48] studied the bimaterial strip subjected to uniform temperature change using PD in conjunction with an adaptive dynamic relaxation (ADR) solver. Oterkus et al. [42] employed PD to investigate the temperature distribution over a plate made of two different materials with an insulated interface crack. A formal discussion about material interfaces in PD was made by Alali and Gunzburger [49], and they showed that the operator of linear PD diverges from the local solution in the limit of vanishing nonlocality when material properties are discontinuous. Bimaterial interface fracture was conducted by Wang et al. [50] with the use of the weight function method for constructing the interfacial force function. Ren et al. [51] applied dual-horizon PD to simulate crack propagation in heterogeneous materials. An OSB-PD model was presented to predict damage growth of bimaterial structures under thermomechanical loading by Zhang and Qiao [52]. Alebrahim [53] proposed a PD model to examine Lamb wave propagation in bimaterial plates. A weak form of bond-associated NOSB-PD was formulated by Behera et al. [54] to analyze damage initiation and its growth in bonded lap joints of dissimilar materials. Recently, new PD homogenization approaches were developed by Xia et al. [55] and Madenci et al. [56] to obtain the effective properties of microstructures with defects, and they demonstrated that PD is absolutely suitable for modeling structures with multiple geometric and material discontinuities.

In fact, these previous studies suggested various techniques for modeling the material interface in PD, but they do not rigorously examine the accuracy of solutions at the interface region. Therefore, this study aims at reviewing different methods for modeling the material interface in PD and checking the accuracy of solutions at material interfaces as compared with local theory, e.g., CCM.

The remainder of the paper is outlined as follows. In Section 2, the OSB-PD theory and bimaterial modeling are reviewed. Next, PDDO is briefly introduced for the calculation of displacement derivatives in Section 2.4. In order to verify the performance of different bimaterial modeling techniques in PD, benchmark problems are carried out in Section 3. In Section 4, numerical examples, consisting of static and dynamic cases, are presented to illustrate the capabilities of OSB-PD in structural modeling with multiple defects.

2 Ordinary state-based peridynamics

2.1 Formulation

PD is a nonlocal theory first introduced by Silling [30] and later generalized by Silling et al. [31] as a reformulation of CCM to resolve problems involving discontinuities and long-range forces. In PD, a material point is considered to interact with other points within a finite distance δ. As shown in Fig. 1, a material point, initially located at $\boldsymbol{x}$, is associated with its own family $H_{\boldsymbol{x}}$, and it interacts with other family members $\boldsymbol{x'}$ through bonds. Similarly, material points $\boldsymbol{x'}$ also interacts with other material points in their own families $H_{\boldsymbol{x'}}$. The relative position vector between $\boldsymbol{x}$ and $\boldsymbol{x'}$ is defined as $\boldsymbol{\xi} = \boldsymbol{x'} - \boldsymbol{x}$. During the deformation, the material points $\boldsymbol{x}$ and $\boldsymbol{x'}$ undergo displacements $\boldsymbol{u}$ and $\boldsymbol{u'}$, respectively. Furthermore, the positions of $\boldsymbol{x}$ and $\boldsymbol{x'}$ in the deformed state can be specified as $\boldsymbol{y} = \boldsymbol{x} + \boldsymbol{u}$ and $\boldsymbol{y'} = \boldsymbol{x'} + \boldsymbol{u'}$.

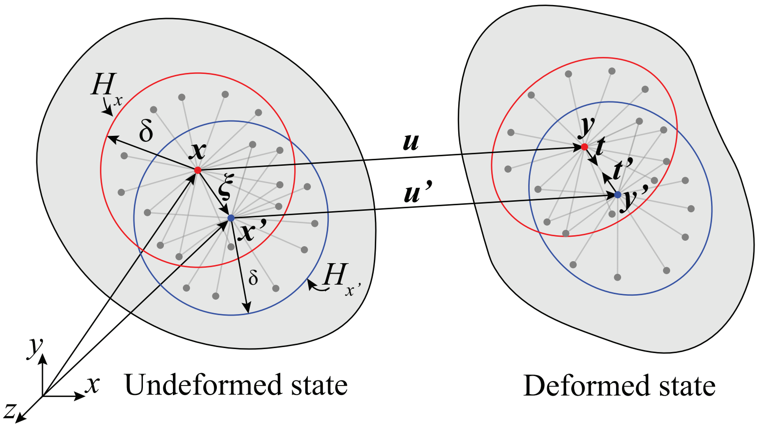

Fig. 1 Nonlocal interactions between material points $\boldsymbol{x}$ and $\boldsymbol{x'}$, and the resulting force density vectors

As derived by Silling [30, 31] and later by Madenci and Oterkus [45], at any instant of time t, the PD equations of motion at a material point, $\boldsymbol{x}$, can be expressed as

$$\rho(\boldsymbol{x})\ddot{\boldsymbol{u}}(\boldsymbol{x},t) = \int_{H_{\boldsymbol{x}}} (\boldsymbol{t}(\boldsymbol{u'}-\boldsymbol{u},\boldsymbol{x'}-\boldsymbol{x},t) - \boldsymbol{t'}(\boldsymbol{u}-\boldsymbol{u'},\boldsymbol{x}-\boldsymbol{x'},t))dH + \boldsymbol{b}(\boldsymbol{x},t), \tag{1}$$

where ρ is the mass density, $\ddot{\boldsymbol{u}}$ is the acceleration, $\boldsymbol{b}$ is the body force density vector. $H_{\boldsymbol{x}}$ denotes the horizon or the interaction domain of a material point located at position $\boldsymbol{x}$. The shape of a family can be represented by a sphere (3D), cylinder (2D), or line (1D), and the family size can be characterized by δ. In OSB-PD, the deformation of a bond depends not only on the deformation of that bond itself but also on the collective deformation of other bonds, and the interactions between material points $\boldsymbol{x}$ and $\boldsymbol{x'}$ result in the force density vector $\boldsymbol{t}$ and $\boldsymbol{t'}$, which represent the force that $\boldsymbol{x'}$ exerts on $\boldsymbol{x}$ and the force that $\boldsymbol{x}$ exerts on $\boldsymbol{x'}$, respectively. Note that the force density vectors, $\boldsymbol{t}$ and $\boldsymbol{t'}$, can have unequal magnitudes and are required to be parallel to the relative position vector in the deformed state in OSB-PD. This requirement is essential to satisfy the balance of angular momentum in OSB-PD as proven by Silling [31].

Based on the derivation of Madenci and Oterkus [45], the PD force density vector can be achieved if the explicit form of the strain energy density (SED) function is known, and it can be written as

$$\boldsymbol{t}(\boldsymbol{u'}-\boldsymbol{u},\boldsymbol{x'}-\boldsymbol{x},t)=\frac{1}{V'}\frac{\partial W}{\partial|\boldsymbol{y'}-\boldsymbol{y}|}\frac{\boldsymbol{y'}-\boldsymbol{y}}{|\boldsymbol{y'}-\boldsymbol{y}|}, \tag{2}$$

in which W is the SED at point $\boldsymbol{x}$ and V' is the volume of material point $\boldsymbol{x'}$.

For an isotropic linear elastic material, the PD form of the SED function at point $\boldsymbol{x}$ is suggested by Madenci and Oterkus [45] as

$$W(\boldsymbol{x})=a\theta^2+b\int_{H_{\boldsymbol{x}}}w(|\boldsymbol{\xi}|)(|\boldsymbol{y'}-\boldsymbol{y}|-|\boldsymbol{\xi}|)^2dV. \tag{3}$$

The dilatation θ at point $\boldsymbol{x}$ can be expressed as

$$\theta=d\int_{H_{\boldsymbol{x}}}w(|\boldsymbol{\xi}|)(|\boldsymbol{y'}-\boldsymbol{y}|-|\boldsymbol{\xi}|)\Lambda dV, \tag{4}$$

where

$$\Lambda=\frac{\boldsymbol{y'}-\boldsymbol{y}}{|\boldsymbol{y'}-\boldsymbol{y}|}\cdot\frac{\boldsymbol{x'}-\boldsymbol{x}}{|\boldsymbol{x'}-\boldsymbol{x}|}, \tag{5}$$

and the weight function, which specifies the degree of interaction between material points, is given in the form [45]

$$w(|\boldsymbol{\xi}|)=\frac{\delta}{|\boldsymbol{x'}-\boldsymbol{x}|}. \tag{6}$$

The PD parameters a, b, and d in Eqs. (3) and (4) can be determined in terms of engineering material properties, e.g., bulk modulus κ and shear modulus μ, by considering two simple loading conditions: isotropic expansion and simple shear. For a 2D analysis, the specific forms of these PD parameters can be given as [45,60]

$$a=\frac{1}{2}(\kappa-2\mu),\quad b=\frac{6\mu}{\pi h\delta^4},\quad d=\frac{2}{\pi h\delta^3}, \tag{7}$$

for plane stress, and

$$a=\frac{\mu(3\kappa-5\mu)}{6\mu-2\kappa},\quad b=\frac{6\mu}{\pi h\delta^4},\quad d=\frac{2}{\pi h\delta^3}, \tag{8}$$

for plane strain.

The bulk modulus κ and shear modulus μ are related to Young's modulus E and Poisson's ratio ν in a 2D case as

$$\kappa=\frac{E}{2(1-\nu)},\quad \mu=\frac{E}{2(1+\nu)}. \tag{9}$$

It should be noted that the PD parameters in Eqs. (7) and (8) are derived for material points whose horizons are completely embedded inside a homogeneous material. For material points close to the boundaries or interfaces, their stiffness might be softer or stiffer than those in the bulk, so they need to be corrected to compensate for the incomplete horizon.

Using the representation of the SED given in Eq. (3) and the weight function specified in Eq. (6), the force density vector $\boldsymbol{t}$ can be formulated by Madenci and Oterkus [45] as

$$\boldsymbol{t}(\boldsymbol{u'}-\boldsymbol{u},\boldsymbol{x'}-\boldsymbol{x},t)=\left(2ad\delta\frac{\theta}{|\boldsymbol{\xi}|}\Lambda+2\delta b\frac{|\boldsymbol{y'}-\boldsymbol{y}|-|\boldsymbol{\xi}|}{|\boldsymbol{\xi}|}\right)\frac{\boldsymbol{y'}-\boldsymbol{y}}{|\boldsymbol{y'}-\boldsymbol{y}|}. \tag{10}$$

2.2 Bimaterial modeling

For a body consisting of dissimilar materials, a bond can connect material points belonging either to the same material or to different materials. Therefore, the bond properties not only needs to be defined for individual materials but also for the interface. As shown in Fig. 2, if a domain is comprised of two different materials, there are three bond properties that need to be specified, i.e., two for the interactions between points having the same material and one for the interaction across the interface. Particularly, for bonds connecting material points with the same material, the properties of the bonds are chosen to be those of the material points. For bonds extending across the interface, their properties can be specified in various approaches as follows.

As suggested by Kilic and Madenci [48], the properties of the material with smaller bulk modulus are used for determining bond properties. Consequently, when the force density vectors, $\boldsymbol{t}$ and $\boldsymbol{t}'$, in Eq. (1) are obtained, the smaller value of the bulk moduli of the two materials is utilized to compute the PD parameters.

Alternatively, the material properties in the domain can be expressed in the form of Heaviside functions as considered by Behera et al. [54],

$$\alpha(x) = \alpha_1 H(-x) + \alpha_2 H(x), \tag{11}$$

where $H(x)$ is the Heaviside function, and α is the material property, e.g., bulk modulus, shear modulus, Young's modulus, or Poisson's ratio. Subscripts 1 and 2 indicate material 1 and material 2, respectively. This method simply implies that when the force density vector $\boldsymbol{t}$ in Eq. (1) is calculated, the material properties of point $\boldsymbol{x}$ are used for the evaluation of PD parameters. Similarly, when the force density vector $\boldsymbol{t}'$ in Eq. (1) is obtained, the material properties of point $\boldsymbol{x}'$ are used for the evaluation of PD parameters.

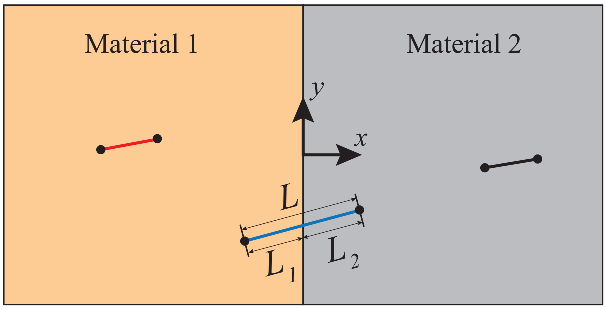

Fig. 2 Interactions between two material points in the presence of a material interfaces. The red bond and black bond denote the interaction between material points in material 1 and in material 2, respectively. The blue bond represents the interaction between material points across the interface

Another technique, which can be used to model the bimaterial interface in PD, is bond average as recommended by Oterkus [42], Wang et al. [50], Behera et al. [54]. The bond average technique can be classified into two types, e.g., arithmetic average and harmonic average.

For the arithmetic average, the average material property of a bond can be approximated as

$$\alpha = \frac{\alpha_1 L_1 + \alpha_2 L_2}{L}. \tag{12}$$

For the harmonic average, the average material property of a bond can be achieved as

$$\alpha = \frac{L}{\frac{L_1}{\alpha_1} + \frac{L_2}{\alpha_2}}, \tag{13}$$

where L_1 denotes the length of the bond in material 1, L_2 denotes the length of the bond in material 2, and $L = L_1 + L_2$ is the total length of the bond as shown in Fig. 2.

It is worth noting that when material 1 and 2 are the same, the aforementioned interface modeling approaches reduce to a single material, so it avoids using separate treatment for homogeneous and inhomogeneous cases.

2.3 Numerical implementation

Since the PD equation of motion Eq. (1) is an integro-differential equation, it is not usually feasible for analytic solutions. Therefore, its solution can be sought by using numerical techniques for spatial and time integration. For the spatial discretization, the collocation method of a meshless scheme [45, 57] can be employed due to its simplicity. As shown in Fig. 3, the domain of interest is divided into finite cells, and each cell is considered as a single integration point located at its mass center associated with material properties and volume. As a result, Eq. (1) is spatially discretized as

$$\rho(\boldsymbol{x}_k)\ddot{\boldsymbol{u}}(\boldsymbol{x}_k,t)=\sum_{j=1}^{N}[\boldsymbol{t}_{kj}(\boldsymbol{u}_j-\boldsymbol{u}_k,\boldsymbol{x}_j-\boldsymbol{x}_k,t)-\boldsymbol{t}_{jk}(\boldsymbol{u}_k-\boldsymbol{u}_j,\boldsymbol{x}_k-\boldsymbol{x}_j,t)]V_j+\boldsymbol{b}(\boldsymbol{x}_k,t), \tag{14}$$

where N represents the total number of material points j within the horizon of material point k, and V_j indicates the volume of material point j. The central difference scheme is adopted for the time integration. With the use of the central difference scheme, Eq. (14) becomes

$$\boldsymbol{u}_k^{n+1}=\frac{\Delta t^2}{\rho}[\sum_{j=1}^{N}(\boldsymbol{t}_{kj}^n-\boldsymbol{t}_{jk}^n)V_j+\boldsymbol{b}_k^n]+2\boldsymbol{u}_k^n-\boldsymbol{u}_k^{n-1}, \tag{15}$$

in which n is the time step number and Δt is the time step size. Generally, an explicit scheme like central difference method requires small time steps to ensure stability as well as accuracy, so it may not be appropriate for obtaining the static solution. Hence, an ADR method [48] can be utilized in order to achieve the static solution.

Since the surface effect affects the accuracy of solutions near the boundaries and interfaces, the surface correction is needed. In this study, the energy method [45] is employed to reduce the surface effect. Furthermore, the volume correction technique [45] is also used to enhance the solution.

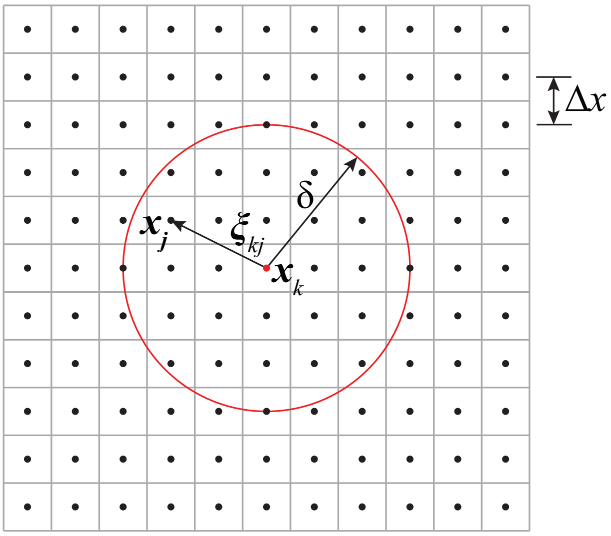

Fig. 3 Domain discretization

2.4 Peridynamic differential operator

Recently, the PDDO was introduced by Madenci et al. [47] to convert the local differential operator to its nonlocal integral form. The PDDO enables the accurate determination of arbitrary-order derivatives of a function without performing any differentiation by employing the nonlocal interaction concept and orthogonal functions [47]. In this paper, only the PDDO for derivatives up to second order of a function with two independent variables is presented. For more details of PDDO, see [47].

Consider a scalar function with two variables, $f(\boldsymbol{x}) = f(x, y)$, the Taylor series expansion of this function at point $\boldsymbol{x}$ can be expanded as

$$\begin{aligned} f(\boldsymbol{x}+\boldsymbol{\xi}) = f(\boldsymbol{x}) + \xi_1 \frac{\partial f(\boldsymbol{x})}{\partial x} + \xi_2 \frac{\partial f(\boldsymbol{x})}{\partial y} + \frac{1}{2!}\xi_1^2 \frac{\partial^2 f(\boldsymbol{x})}{\partial x^2} + \\ \frac{1}{2!}\xi_2^2 \frac{\partial^2 f(\boldsymbol{x})}{\partial y^2} + \xi_1\xi_2 \frac{\partial^2 f(\boldsymbol{x})}{\partial x \partial y} + R, \end{aligned} \tag{16}$$

where R represents the higher-order term which is negligibly small. In order to derive the PD nonlocal expression for the partial derivatives, multiply each term in Eq. (16) with PD functions, $g^{p_1 p_2}(\boldsymbol{\xi})$ and integrate over the interaction domain $H_{\boldsymbol{x}}$, it yields

$$\begin{aligned} \int_{H_{\boldsymbol{x}}} f(\boldsymbol{x}+\boldsymbol{\xi}) g^{p_1 p_2}(\boldsymbol{\xi}) dV = f(\boldsymbol{x}) \int_{H_{\boldsymbol{x}}} g^{p_1 p_2}(\boldsymbol{\xi}) dV + \frac{\partial f(\boldsymbol{x})}{\partial x} \int_{H_{\boldsymbol{x}}} \xi_1 g^{p_1 p_2}(\boldsymbol{\xi}) dV + \\ \frac{\partial f(\boldsymbol{x})}{\partial y} \int_{H_{\boldsymbol{x}}} \xi_2 g^{p_1 p_2}(\boldsymbol{\xi}) dV + \frac{\partial^2 f(\boldsymbol{x})}{\partial x^2} \int_{H_{\boldsymbol{x}}} \frac{1}{2!}\xi_1^2 g^{p_1 p_2}(\boldsymbol{\xi}) dV + \\ \frac{\partial^2 f(\boldsymbol{x})}{\partial y^2} \int_{H_{\boldsymbol{x}}} \frac{1}{2!}\xi_2^2 g^{p_1 p_2}(\boldsymbol{\xi}) dV + \frac{\partial^2 f(\boldsymbol{x})}{\partial x \partial y} \int_{H_{\boldsymbol{x}}} \xi_1 \xi_2 g^{p_1 p_2}(\boldsymbol{\xi}) dV, \end{aligned} \tag{17}$$

where p_1 and p_2 denote the order of differentiation with respect to x and y, respectively.

According to Madenci et al. [47], the PD functions are constructed so that they posses the orthogonality properties as

$$\frac{1}{n_1! n_2!} \int_{H_{\boldsymbol{x}}} \xi_1^{n_1} \xi_2^{n_2} g^{p_1 p_2}(\boldsymbol{\xi}) dV = \delta_{n_1 p_1} \delta_{n_2 p_2}, \tag{18}$$

with $(n_1, n_2, p_1, p_2 = 0, 1, 2)$, and $\delta_{n_1 p_1}$ and $\delta_{n_2 p_2}$ are the Kronecker delta functions.

Enforcing the orthogonality property of PD functions into Eq. (17) results in the nonlocal expressions for the function itself and its derivatives as

$$\frac{\partial^{p_1+p_2} f(\boldsymbol{x})}{\partial x^{p_1} \partial y^{p_2}} = \int_{H_{\boldsymbol{x}}} f(\boldsymbol{x}+\boldsymbol{\xi}) g^{p_1 p_2}(\boldsymbol{\xi}) dV. \tag{19}$$

The PD functions, $g^{p_1 p_2}$, can be constructed as a polynomial function as [47]

$$\begin{aligned} g^{p_1 p_2}(\boldsymbol{\xi}) = a_{00}^{p_1 p_2} w(|\boldsymbol{\xi}|) + a_{10}^{p_1 p_2} w(|\boldsymbol{\xi}|)\xi_1 + a_{01}^{p_1 p_2} w(|\boldsymbol{\xi}|)\xi_2 + \\ a_{20}^{p_1 p_2} w(|\boldsymbol{\xi}|)\xi_1^2 + a_{02}^{p_1 p_2} w(|\boldsymbol{\xi}|)\xi_2^2 + a_{22}^{p_1 p_2} w(|\boldsymbol{\xi}|)\xi_1\xi_2, \end{aligned} \tag{20}$$

where $a_{q_1 q_2}^{p_1 p_2}$ are the unknown coefficients with $(q_1, q_2 = 0, 1, 2)$ and $w(|\boldsymbol{\xi}|)$ is the weight function. Generally, the weight function can be chosen to have the same form as Eq. (6) or can be specified as a Gaussian distribution [47], e.g., $w(|\boldsymbol{\xi}|) = e^{-(2|\boldsymbol{\xi}|/\delta)^2}$.

Substituting this representation of PD functions into the orthogonality equation, Eq. (18), leads to a system of equations for obtaining the coefficients $a_{q_1 q_2}^{p_1 p_2}$ as

$$\boldsymbol{A}\boldsymbol{a} = \boldsymbol{b}, \tag{21}$$

in which

$$\boldsymbol{A} = \int_{\boldsymbol{H_x}} w(|\boldsymbol{\xi}|) \begin{bmatrix} 1 & \xi_1 & \xi_2 & \xi_1^2 & \xi_2^2 & \xi_1\xi_2 \\ \xi_1 & \xi_1^2 & \xi_1\xi_2 & \xi_1^3 & \xi_1\xi_2^2 & \xi_1^2\xi_2 \\ \xi_2 & \xi_1\xi_2 & \xi_2^2 & \xi_1^2\xi_2 & \xi_2^3 & \xi_1\xi_2^2 \\ \xi^2 & \xi_1^3 & \xi_1^2\xi_2 & \xi_1^4 & \xi_1^2\xi_2^2 & \xi_1^3\xi_2 \\ \xi_2^2 & \xi_1\xi_2^2 & \xi_2^3 & \xi_1^2\xi_2^2 & \xi_2^4 & \xi_1\xi_2^3 \\ \xi_1\xi_2 & \xi_1^2\xi_2 & \xi_1\xi_2^2 & \xi_1^3\xi_2 & \xi_1\xi_2^3 & \xi_1^2\xi_2^2 \end{bmatrix} dV, \tag{22}$$

$$\boldsymbol{a} = \begin{bmatrix} a_{00}^{00} & a_{00}^{10} & a_{00}^{01} & a_{00}^{20} & a_{00}^{02} & a_{00}^{11} \\ a_{10}^{00} & a_{10}^{10} & a_{10}^{01} & a_{10}^{20} & a_{10}^{02} & a_{10}^{11} \\ a_{01}^{00} & a_{01}^{10} & a_{01}^{01} & a_{01}^{20} & a_{01}^{02} & a_{01}^{11} \\ a_{20}^{00} & a_{20}^{10} & a_{20}^{01} & a_{20}^{20} & a_{20}^{02} & a_{20}^{11} \\ a_{02}^{00} & a_{02}^{10} & a_{02}^{01} & a_{02}^{20} & a_{02}^{02} & a_{02}^{11} \\ a_{11}^{00} & a_{11}^{10} & a_{11}^{01} & a_{11}^{20} & a_{11}^{02} & a_{11}^{11} \end{bmatrix}, \ \boldsymbol{b} = \begin{bmatrix} 1 & 0 & 0 & 0 & 0 & 0 \\ 0 & 1 & 0 & 0 & 0 & 0 \\ 0 & 0 & 1 & 0 & 0 & 0 \\ 0 & 0 & 0 & 2 & 0 & 0 \\ 0 & 0 & 0 & 0 & 2 & 0 \\ 0 & 0 & 0 & 0 & 0 & 1 \end{bmatrix}. \tag{23}$$

The matrices $\boldsymbol{A}$ and $\boldsymbol{b}$ are known, and the matrix $\boldsymbol{a}$ contains the unknown coefficients of the PD functions. After the Eq. (21) is solved for the unknown coefficients $\boldsymbol{a}$, the PD functions can be constructed in accordance with Eq. (20).

If the value of $f(\boldsymbol{x})$ is known in Eq. (16), the PD functions $g^{p_1 p_2}$ can be constructed for $f(\boldsymbol{x}+\boldsymbol{\xi}) - f(\boldsymbol{x})$ [47]. As a result, the range of n_i, p_i and q_i does not include zero. In other words, the first row and the first column of $\boldsymbol{A}, \boldsymbol{a}$ and $\boldsymbol{b}$ are removed. In this case, the gradient of $f(\boldsymbol{x})$ is

$$\nabla f(\boldsymbol{x}) = \begin{Bmatrix} \frac{\partial f(\boldsymbol{x})}{\partial x} \\ \frac{\partial f(\boldsymbol{x})}{\partial y} \end{Bmatrix} = \int_{H_{\boldsymbol{x}}} (f(\boldsymbol{x}+\boldsymbol{\xi}) - f(\boldsymbol{x})) \begin{Bmatrix} g^{10}(\boldsymbol{\xi}) \\ g^{01}(\boldsymbol{\xi}) \end{Bmatrix} dV. \tag{24}$$

Similarly, the gradient of a vector function, $\boldsymbol{f}(\boldsymbol{x})$ can be expressed as

$$\nabla \boldsymbol{f}(\boldsymbol{x}) = \begin{bmatrix} \frac{\partial f_1(\boldsymbol{x})}{\partial x} & \frac{\partial f_1(\boldsymbol{x})}{\partial y} \\ \frac{\partial f_2(\boldsymbol{x})}{\partial x} & \frac{\partial f_2(\boldsymbol{x})}{\partial y} \end{bmatrix} = \int_{H_{\boldsymbol{x}}} (\boldsymbol{f}(\boldsymbol{x}+\boldsymbol{\xi}) - \boldsymbol{f}(\boldsymbol{x})) \otimes \begin{Bmatrix} g^{10}(\boldsymbol{\xi}) \\ g^{01}(\boldsymbol{\xi}) \end{Bmatrix} dV. \tag{25}$$

where $\otimes$ is the dyadic product between two vectors.

In this study, the PDDO is employed to compute the gradient of the displacement field $\nabla \boldsymbol{u}$. After the displacement solution is obtained by solving the PD equations of motion, the displacement gradient can be obtained by using Eq. (25). For small displacement and rotation, the infinitesimal strains can be obtained as

$$\boldsymbol{\varepsilon} = \frac{1}{2}(\nabla \boldsymbol{u} + \nabla^T \boldsymbol{u}). \tag{26}$$

in which $\boldsymbol{\varepsilon}$ is the strain tensor and $\nabla^T \boldsymbol{u}$ is the transpose of $\nabla \boldsymbol{u}$.

3 Benchmark problems

The accuracy of various PD bimaterial modeling techniques introduced in Section 2.2 is examined through two static problems: plate under tension and plate under shear. Consider a rectangular plate with a bimaterial interface located at the vertical center line as illustrated in Fig. 4. The Young's modulus and Poisson's ratio of each material are as follows: $E_1 = 1{,}000$ GPa, $\nu_1 = 0.3$, $E_2 = 100$ GPa, and $\nu_2 = 0.25$. The plate is fixed at the left end and is subjected to loading, e.g., tension or shear, at the other end. The plate is discretized with the nodal spacing $\Delta x = 0.0025$ m. In the PD model, displacement boundary conditions (BCs) are applied through a fictitious boundary layer with depth equal to the horizon size δ [57], which is chosen to be $3.015\Delta x$. The horizon size, $\delta \approx 3.0\Delta x$ and specifically $\delta = 3.015\Delta x$, is commonly used in PD literature, and it is an optimal value for the majority of problems [57,58]. The traction and shear loading are converted into the body force to apply to the PD material points. In both problems, a plane stress state is assumed, and the ADR [48] is employed to seek the static solution. Furthermore, FEM is used as a reference solution to verify the accuracy of PD solutions, hence, in general the FE analysis is performed with a fine mesh, which conforms to the material interface, to obtain the converged results.

3.1 Plate under tension

The plate under tension problem is considered. Fig. 5 represents the variation of horizontal displacement along the center line $y = 0$. The force density vectors generated by the interactions between material points across the interface are evaluated by the methods presented in Section 2.2. As indicated in Fig. 5(a), the overall solutions predicted by PD generally agree well with those obtained by FEM for all

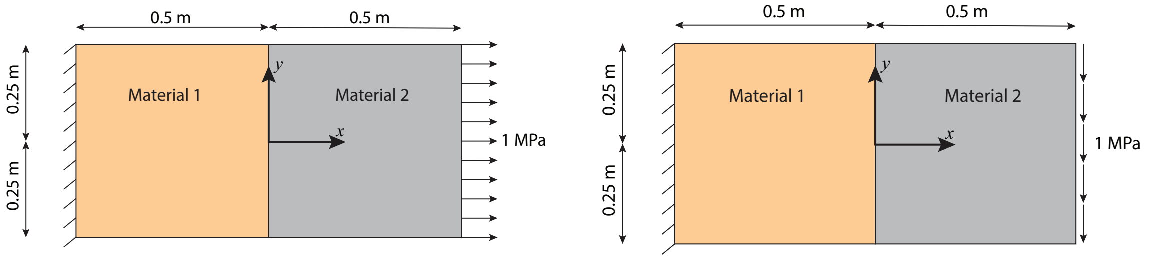

(a) **(b)**

Fig. 4 Bimaterial plate under constant **(a)** tension, **(b)** shear loading

methods. It is well-known that in the CCM the displacement at the interface contains singularity, i.e., discontinuity in strain, due to the difference in material properties, and this non-smooth behaviour is well represented by the FEM solution as shown in Fig. 5. On the other hand, different PD interface modeling techniques exhibit slightly different behaviour at the interface. One noticeable point in Fig. 5(b) is on the left side of the interface the results obtained by different techniques are similar to each other, whereas there are some deviations among them on the right side. Of four approaches, the harmonic average technique shows the best agreement with the local solution. With the use of material having smaller bulk modulus for interface modeling, denoted by "Softer" in Fig. 5, the stiffness of bonds across the interface is generally less stiff, and consequently it leads to higher values of displacement than the local solution. In contrast, both Heaviside and arithmetic average approaches demonstrate slightly stiffer behaviour at the interface, hence, producing lower displacements than FEM.

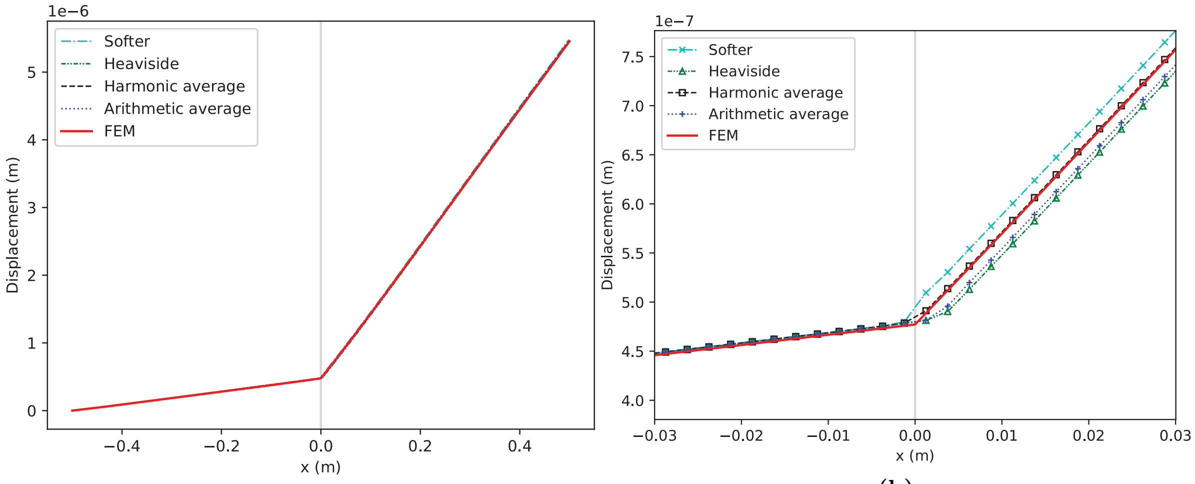

(a) **(b)**

Fig. 5 Horizontal displacement of the plate under tension **(a)** along $y = 0$, **(b)** and its close-up view near the interface at $x = 0$

To have a more rigorous analysis of the accuracy of PD solutions, we would like to compare the PD strain field, obtained by the application of PDDO introduced in Section 2.4, with the FEM strain field. Fig. 6 shows the distribution of normal strain in x-direction along the horizontal center line, i.e., $y = 0$, and near the interface. There exists a close agreement between FEM and PD solution far from the interface, whereas noticeable differences can be seen in the interface region.

The close-up view near the interface in Fig. 6(b) shows how well each PD interface modeling technique can capture the FEM result. As expected, the harmonic average technique has the least "difference" as compared to FEM, and other approaches introduce considerable deviations from the

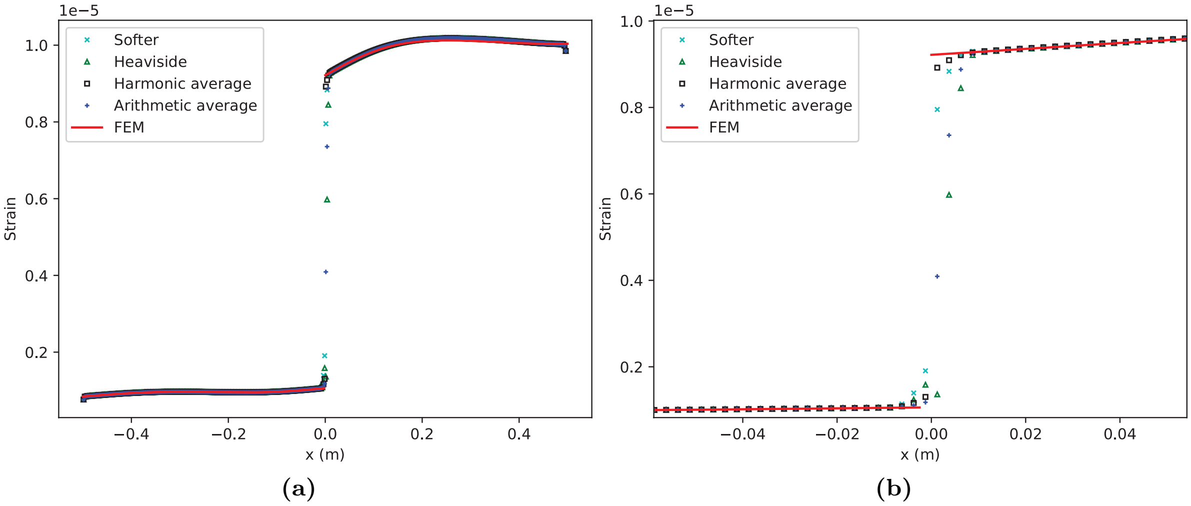

Fig. 6 Normal strain in x-direction **(a)** along $y = 0$, **(b)** and its close-up view near the interface at $x = 0$ for the plate under tension problem

local solution. Here we emphasize on the usage of the word "difference" instead of error in this context. Due to the presence of material discontinuity and a non-smooth field variable, which fails to twice continuously differentiable at the interface, the convergence of the PD model to the local one is not guaranteed [31, 49]. On the one hand, the FEM model is based on the local theory which assumes a material point locally interacts with its closest neighbors. On the other hand, PD is a pure non-local theory, so it takes into account the nonlocal interactions between material points over a finite distance. The difference in the underlying assumptions of the two theories is a possible reason leading to the discrepancy in their predictions of displacements close to the interface. If we look at Fig. 6(b), it can be realized that how nonlocal interactions between material points affect the solution at the interface. In this study, a horizon size of $\delta = 3.015\Delta x$ is chosen, and it means the closest point to the interface shall influence eleven material points in the opposite side of the interface in 2D. As seen from Fig. 6(b), three points nearest to the interface on each side, therefore, have the most significant difference from the FEM solution. One may think that decreasing the horizon size can reduce the interactions between material points near the interface, hence, improving the result at the interface. Actually, it can work for one dimensional cases, but for 2D or 3D dimensional problems, too small horizon sizes have undesirable effects on overall solutions. Discussion about horizon size can be found in [57, 58]. Recently, a few attempts were made to develop nonlocal models which are able to converge to classical models as the horizon size vanishes. Some of them can be found in [49, 59]. Generally, these newly proposed nonlocal models have more complicated implementations than OSB-PD.

It is worth noting that the strain at one material point, which has interactions across the interface, is computed by considering the family points with same material properties only in the evaluation of PDDO. If neighboring points having different material properties are also included, the strains at the interface shall be smoothed out as illustrated in Fig. 7. Additionally, PDDO was shown to yield accurate evaluation of derivatives at material points with non-symmetric families [47]. The accuracy of derivatives is basically not affected by the truncation of horizon near the boundaries or interfaces. Hence, the accuracy of evaluation of strains in this section solely depends on that of displacements obtained by PD.

3.2 Plate under shear

Next the plate under shear loading is examined. Fig. 8 shows horizontal and vertical displacements along the line $y = 0.125$ m. There is a close agreement between FEM and PD predictions.

Furthermore, the close-up views at the interface region are given in Fig. 9. For horizontal displacement, the harmonic average technique is still the one that produces the closest agreement with the

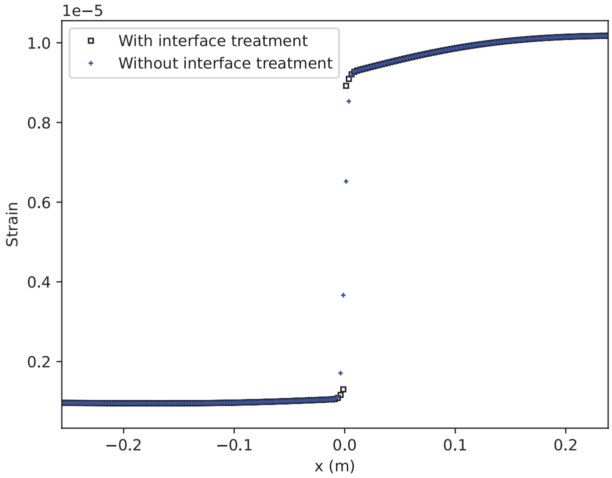

Fig. 7 Normal strain in x-direction with and without material points having different material properties included in PDDO for the harmonic average case

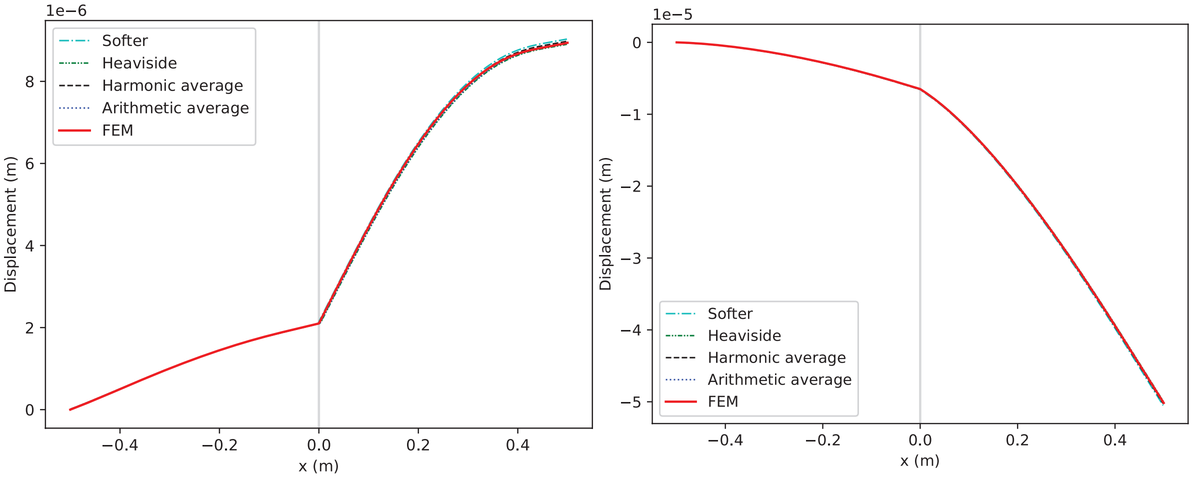

(a) **(b)**

Fig. 8 Displacements of the plate subjected to shear loading along $y = 0.125$ m **(a)** Horizontal displacement, **(b)** Vertical displacement

FEM solution. However, for vertical displacement, arithmetic average and Heaviside techniques give slightly better results than harmonic average approach on the right side of the interface.

Fig. 10 indicates normal strain in x-direction along $y = 0.125$ m. As seen in Fig. 10, the PD solutions accurately capture the FEM solution in the areas away from the interface. Regarding responses at the interface, the difference between PD and FEM results exhibits similar trend to those presented in Section 3.1.

Through the two above examples, it can be concluded that PD solutions obtained by different PD interface modeling approaches are in good agreement with the local solution in the region far from the interface. When it comes to the behaviour close to the interface, the harmonic average technique generally yields the best result as compared to FEM among the four techniques. Therefore, the harmonic average technique will be employed in numerical examples in Section 4.

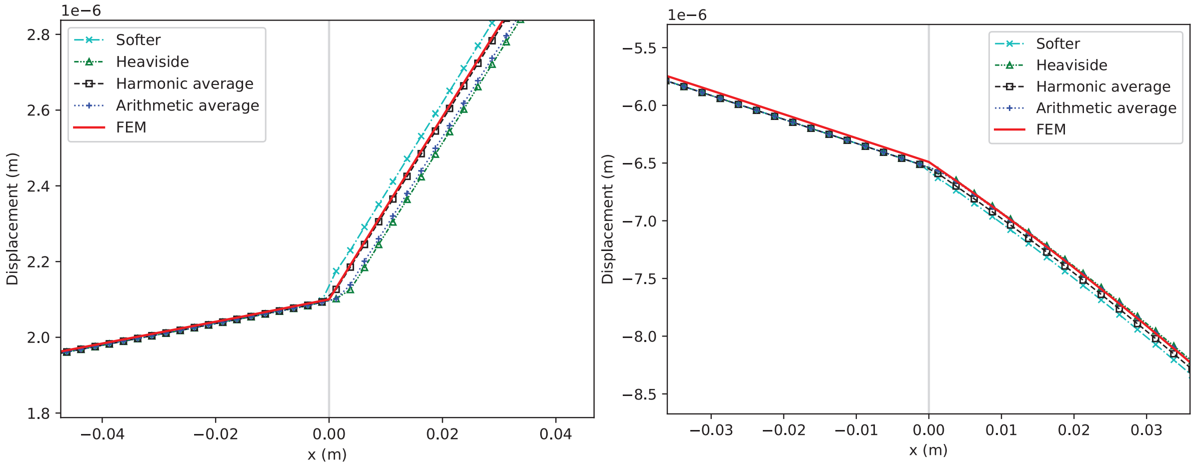

(a) **(b)**

Fig. 9 Close-up view of displacements along $y = 0.125$ m near the interface for the plate under shear loading problem **(a)** Horizontal displacement, and **(b)** Vertical displacement

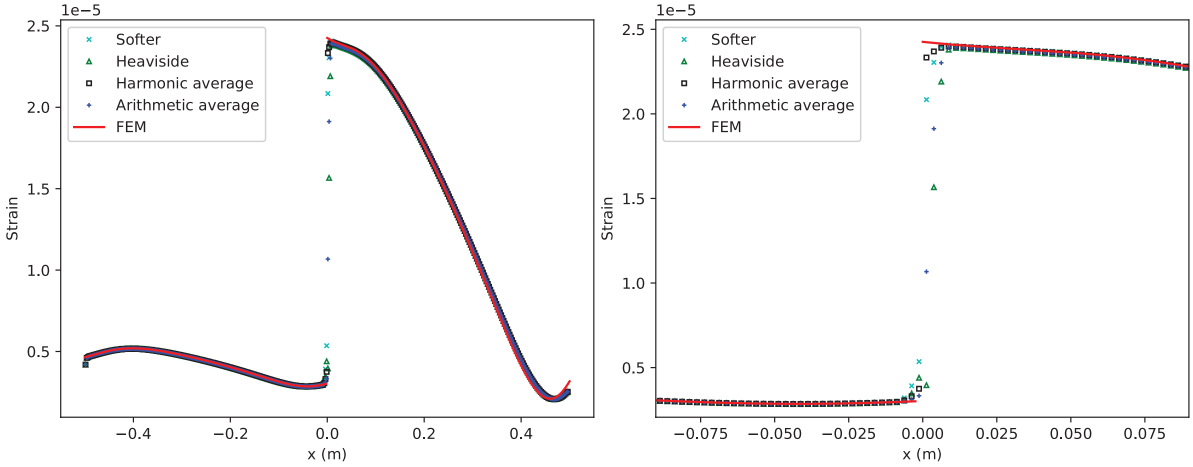

(a) **(b)**

Fig. 10 Normal strain in x-direction **(a)** along $y = 0.125$ m, **(b)** and its close-up view near the interface at $x = 0$ in the plate under shear loading problem

4 Numerical examples

Several numerical examples are presented to illustrate the performance of OSB-PD to model structures with defects, e.g., inclusions or cracks. The first two examples consider a cantilever beam containing a single inclusion subjected to tensile and shear loading. In the third problem, we consider a square plate with two non-symmetric inclusions. In the last example, the effects of inclusions on DSIF are investigated. The first three examples are static problems, so the ADR solver is used. On the other hand, the last example is a dynamic analysis, hence the explicit solver as introduced in Section 2.3 is adopted. Unless otherwise stated, these conditions are considered: (1) Young's moduli of matrix and inclusion are 100 GPa and 10,000 GPa, respectively; (2) Poisson's ratio is 0.3 for matrix and inclusion; (3) Plane stress condition is assumed in static problems, and plane strain condition is assumed in the dynamic analysis; (4) A regular mesh with nodal spacing $\Delta x = 0.0025$ m is used in all numerical examples.

4.1 A cantilever beam with a single inclusion under tensile loading

Consider a cantilever beam containing a single inclusion with a radius of $r = 0.1$ m. The geometry and BCs are indicated in Fig. 11(a). The left edge of the beam is fixed, and the right edge is subjected to a uniform tension loading of 1 MPa. Figs. 12 and 13 show the contours of horizontal and vertical displacements obtained by PD and FEM, respectively. The displacement distribution of PD is in good agreement with that of FEM. Furthermore, the horizontal displacement along $y = 0$ and vertical displacement along $x = 0$ are shown in Fig. 14. The PD solution captures well with the FEM solution. Obviously, the variation of displacements inside the inclusion is much smaller than in the matrix due to the high stiffness of the inclusion.

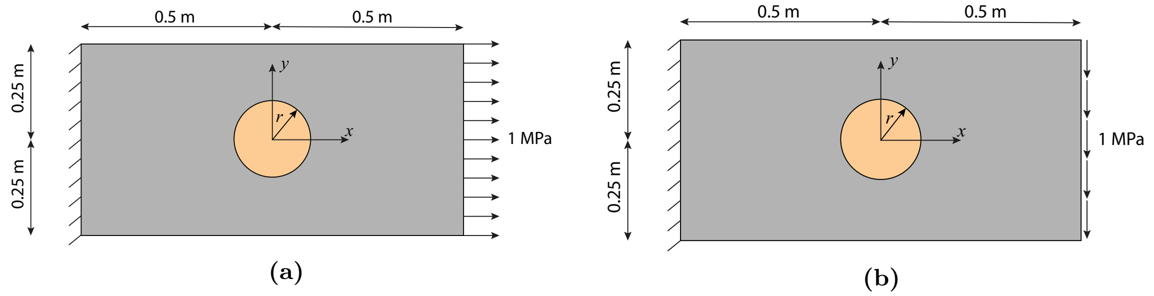

(a) (b)

Fig. 11 Geometry and BCs for the beam with a single-inclusion beam problem **(a)** tension, **(b)** shear loading

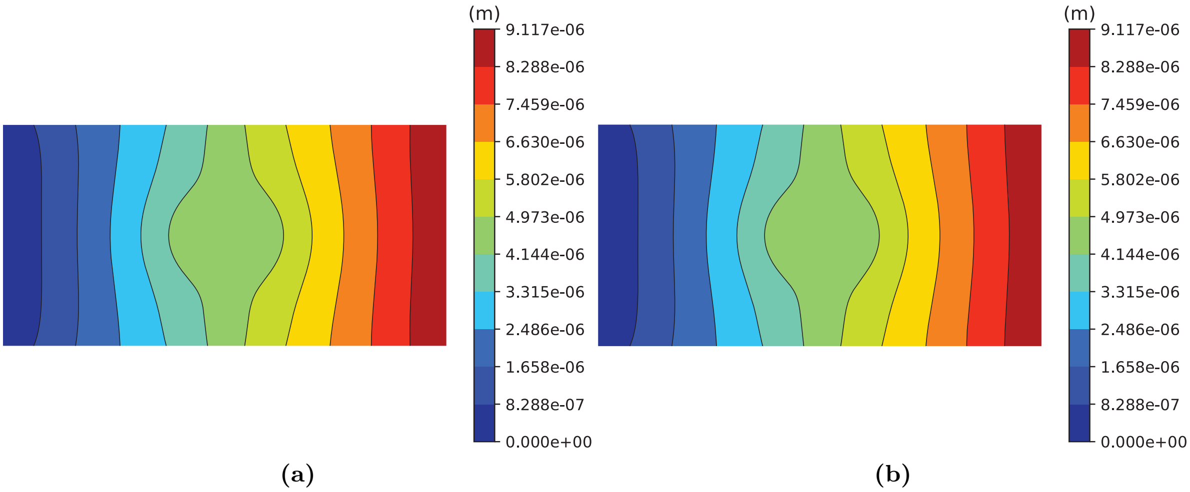

(a) (b)

Fig. 12 Horizontal displacement of a single-inclusion beam subjected to tensile loading **(a)** PD, **(b)** FEM

Fig. 15 illustrates the variations of x-normal strain along $y = 0$ as well as x- and y-normal strains along $x = 0$. As seen from this figure, the strain solution obtained by PD closely agrees with FEM, though there are some noticeable differences between them near the boundaries due to surface effect. Also, Fig. 16 represents the strain distributions obtained by PD. The strains highly concentrate close to the interface between the inclusion and the matrix owing to the mismatch in deformations between them.

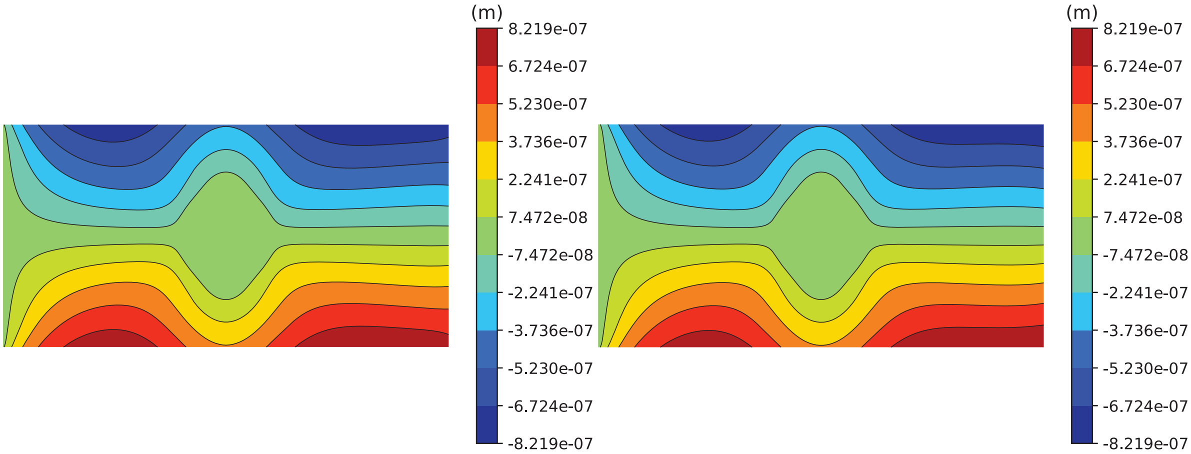

(a) **(b)**

Fig. 13 Vertical displacement of a single-inclusion beam subjected to tensile loading **(a)** PD, **(b)** FEM

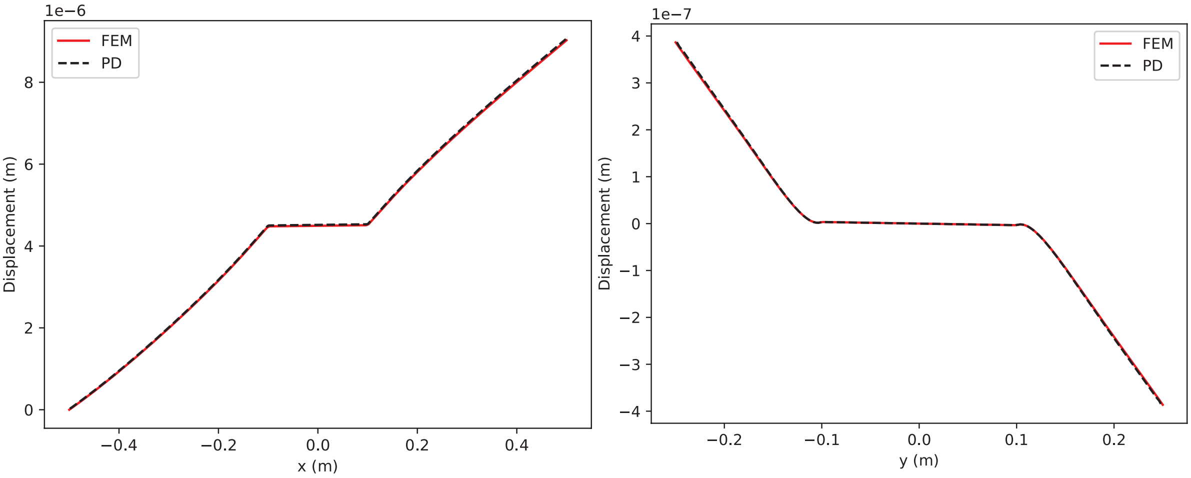

(a) **(b)**

Fig. 14 Variation of displacements in a single-inclusion beam under tensile loading **(a)** Horizontal displacement along $y = 0$, **(b)** Vertical displacement along $x = 0$

4.2 A cantilever beam with a single inclusion under shear loading

The geometry and BCs are similar to those presented in the previous example except that the uniform tension loading is replaced by shear loading of 1 MPa on the right edge of the beam as shown in Fig. 11(b). The comparisons of displacement field are shown in Figs. 17 and 18, and there is a close agreement between PD and FEM. Furthermore, the variations of vertical displacement along $y = 0$ and horizontal displacement along $x = 0$ are illustrated in Fig. 19. As can be seen from this figure, PD predictions reasonably match with those predicted by FEM.

Fig. 20 represents the distributions of strain components along the cross section located at $x = 0$. It can be observed that x-normal strain is continuous along the cross section, whereas there are discontinuities at the interface in the other components of strain. Overall, PD is capable of producing the same predictions as FEM. The PD strain contours in the whole domain are given in Fig. 21.

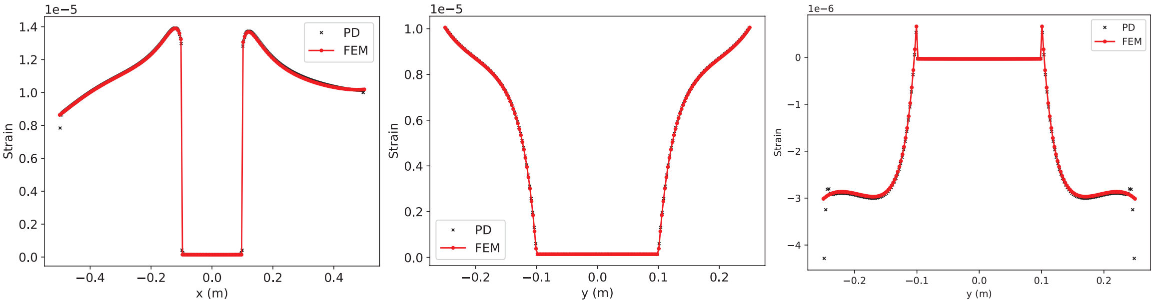

(a) **(b)** **(c)**

Fig. 15 Variations of strains **(a)** x-normal strain along $y = 0$, **(b)** x-normal strain along $x = 0$, **(c)** y-normal strain along $x = 0$

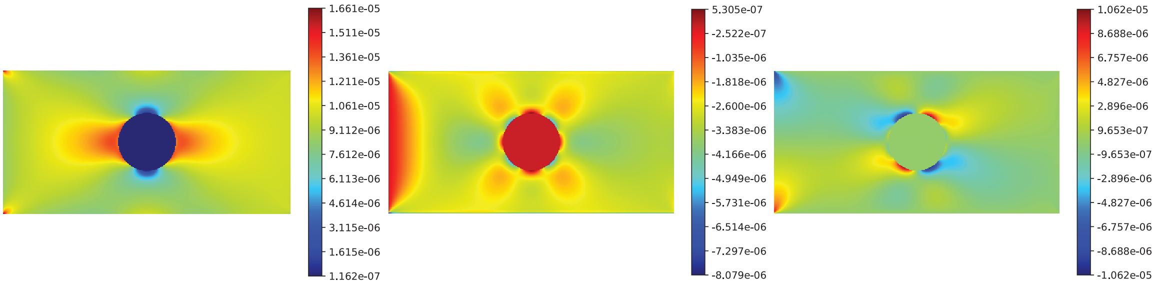

(a) **(b)** **(c)**

Fig. 16 Contours of strain components **(a)** x-normal strain, **(b)** y-normal strain, **(c)** shear strain

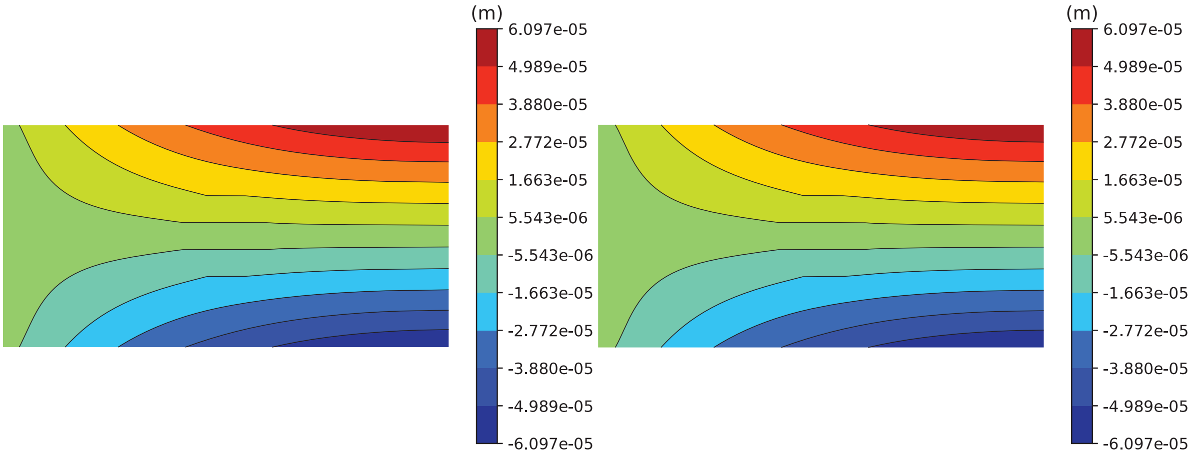

(a) **(b)**

Fig. 17 Horizontal displacement of a single-inclusion beam under shear loading **(a)** PD, **(b)** FEM

4.3 A plate with two non-symmetric circular inclusions

A plane stress unit plate is analyzed. The geometry and BCs are shown in Fig. 22. The model is comprised of two inclusions with different sizes, and the radii of the big and small inclusions are $R = 0.2$ m and $r = 0.1$ m, respectively. A traction of 1 MPa is applied on the right edge, and the left edge is clamped. Figs. 23 and 24 present the deformations achieved by PD and FEM, and the comparison denotes a close agreement between two methods. The displacement smoothly distributes

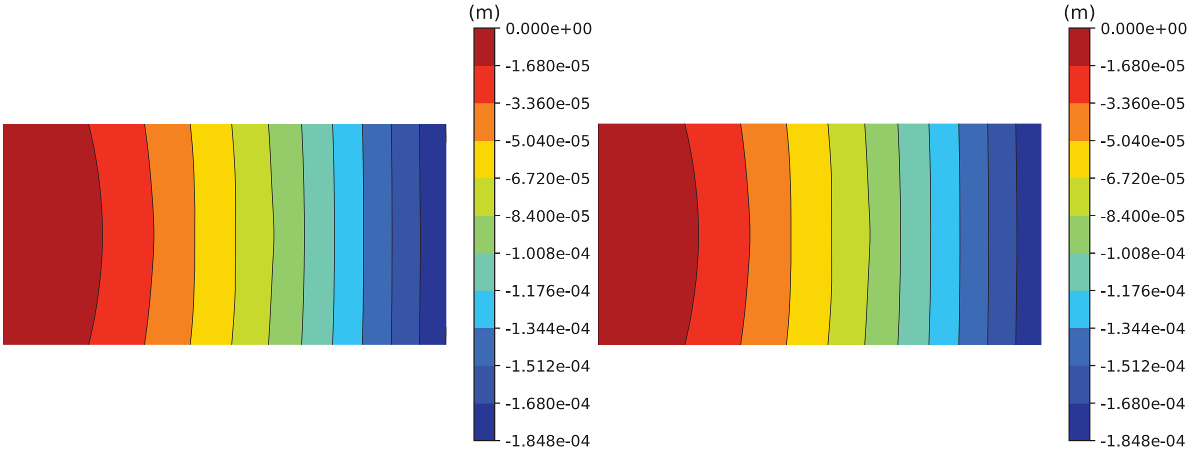

(a) **(b)**

Fig. 18 Vertical displacement of a single-inclusion beam under shear loading **(a)** PD, **(b)** FEM

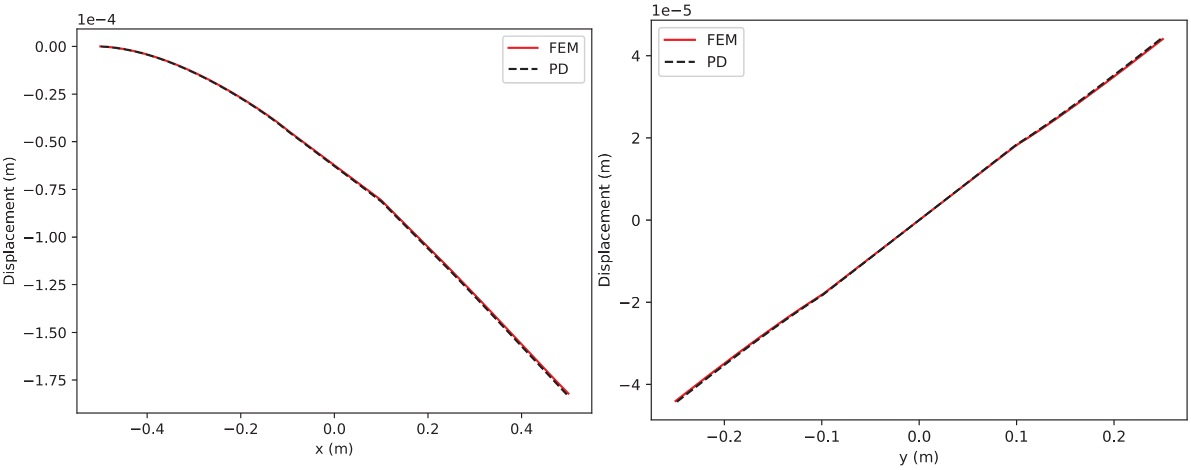

(a) **(b)**

Fig. 19 Variation of displacements in a single-inclusion beam under shear loading **(a)** Vertical displacement along $y = 0$, **(b)** Horizontal displacement along $x = 0$

over the domain in both x- and y-directions, but the deformation pattern is irregular not only due to the presence of inclusions but also due to the asymmetric locations of the inclusions in the model.

Fig. 25 represents the displacements of material points lying along the horizontal and vertical lines passing through the center of the big inclusion, i.e., $y = -0.2$ m and $x = -0.2$ m, respectively. Clearly, the PD solutions match well with those captured by FEM. Generally, the displacement experiences smaller variation in the inclusion than in the matrix. Moreover, the asymmetric positions of the inclusions lead to the downward bending of the plate, even though it is under tension. Also, the displacement components along the diagonal line, $x = y$, is presented in Fig. 26.

The distributions of strains along the lines $x = -0.2$ m and $x = y$ are depicted in Figs. 27 and 28. The differences between two methods can be observed at the interface and at the boundaries. The difference occurring near the boundary regions is mainly due to the surface effect. In addition, a fluctuation of strain values can be recognized in the FEM result in Fig. 28, the reason is the sharp corners of the FEM model cause singularity. At the interface, the nonlocal interactions across the interface result in the differences between FEM and PD; however, these differences are only confined to the local region close to the interface. In other areas, the PD solutions are comparable to the FEM solutions. Fig. 29 shows the distribution of strains computed by PD. Once again, the strains

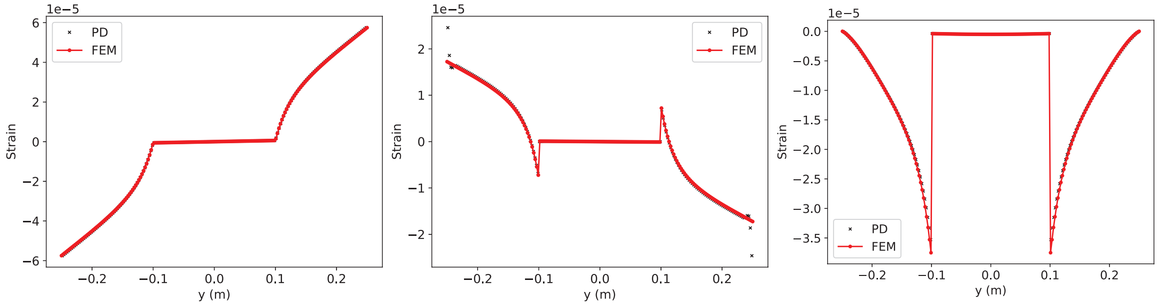

(a) **(b)** **(c)**

Fig. 20 Variations of strains along the cross section at $x = 0$ **(a)** x-normal strain, **(b)** y-normal strain, **(c)** shear strain

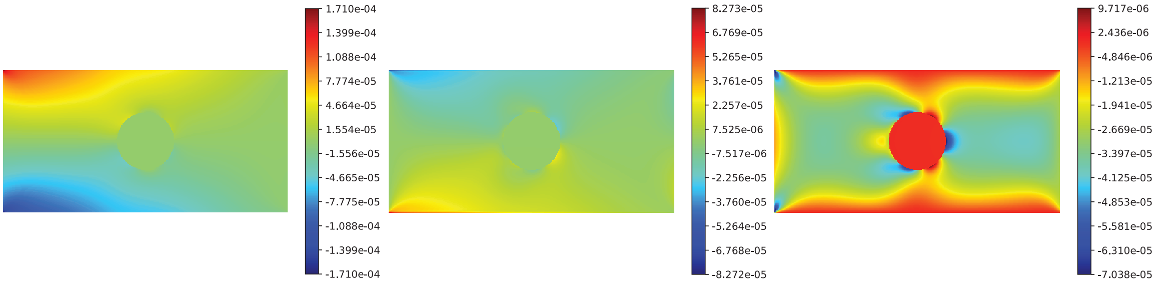

(a) **(b)** **(c)**

Fig. 21 Contours of strain components **(a)** x-normal strain, **(b)** y-normal strain, **(c)** shear strain

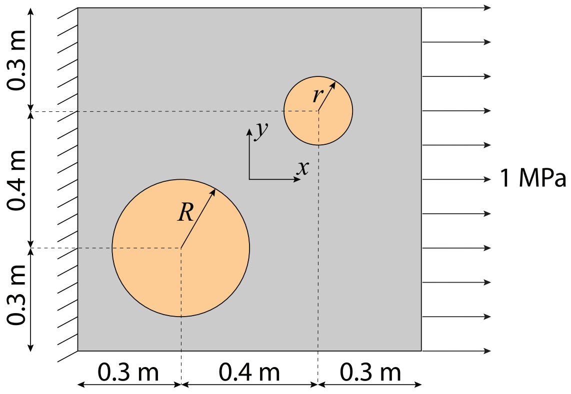

Fig. 22 Geometry and BCs for the plate with two inclusions

are strongly concentrated in the region close to the interface due to the high discrepancy of stiffness between the inclusion and the matrix.

4.4 Effects of the inclusions on the dynamic stress intensity factor in a cracked plate

Consider a rectangular plate containing an inclusion and a central crack as shown in Fig. 30. The height and width of the plate are $h = 40$ mm and $b = 20$ mm, respectively. The central crack has a length of $2a = 4.8$ mm. A step loading of $p(t) = 1$ MPa is imposed on the top and bottom edges of the plate. The ease of modeling cracks is a salient feature in PD because a crack can be formed by simply breaking bonds passing through the crack face. Therefore, the interactions between material points

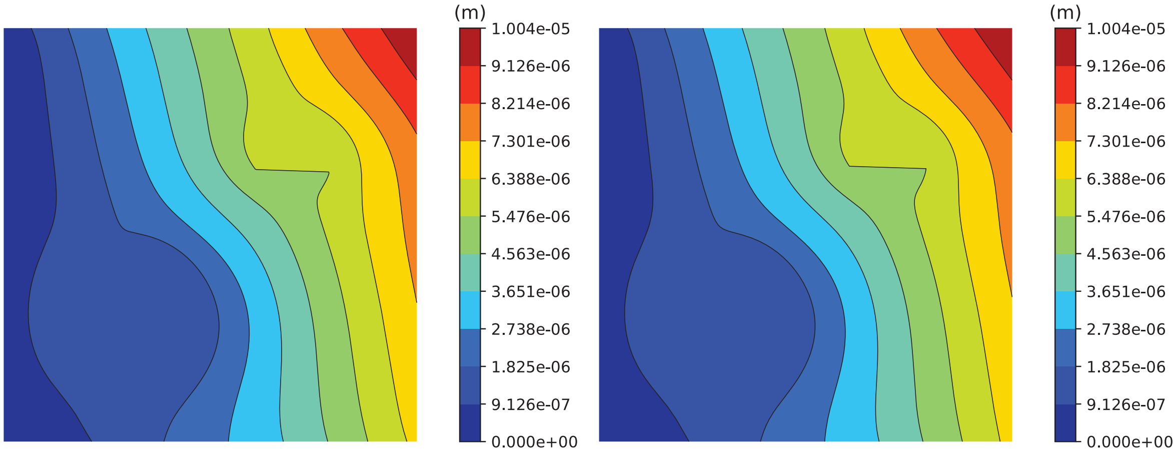

(a) **(b)**

Fig. 23 Horizontal displacement of an asymmetric circular-inclusion plate **(a)** PD, **(b)** FEM

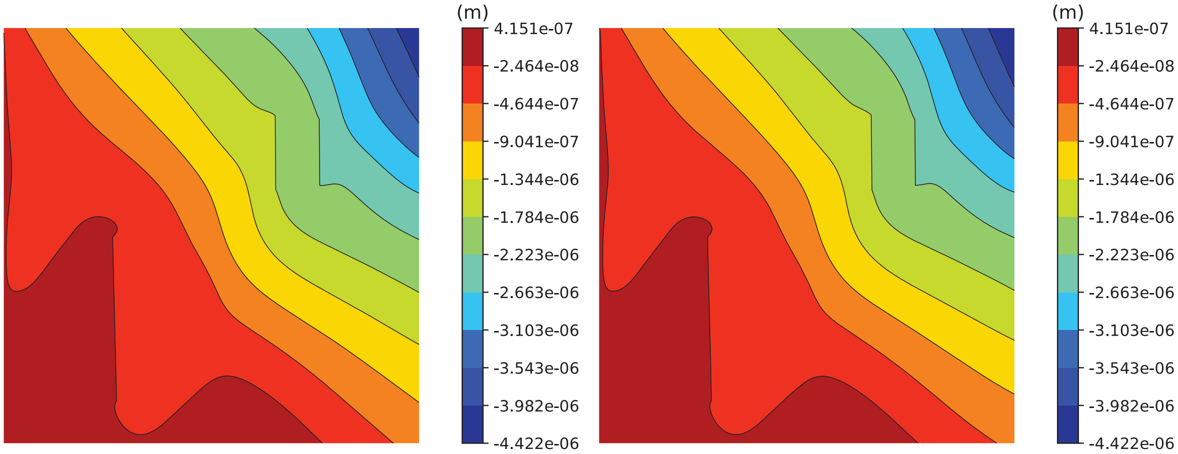

(a) **(b)**

Fig. 24 Vertical displacement of an asymmetric circular-inclusion plate **(a)** PD, **(b)** FEM

across the crack face can be disconnected, and the displacement discontinuity naturally arises. This example demonstrates the effectiveness of PD in modeling structures with different types of defects.

The material properties of the plate are Young's modulus $E = 199.992$ GPa, Poisson's ratio $\nu = 0.3$ and mass density $\rho = 5,000$ kg/m^3. Poison's ratio and mass density of the inclusion are identical to those of the plate, but its Young's modulus E' is varied to study the effects of inclusion stiffness on DSIF. For convenience, we define $\Omega = E'/E$ as the ratio of Young's modulus of the inclusion to Young's modulus of the plate. $\Omega = 1$ corresponds to the case in which the plate contains no inclusion, and $\Omega = 0.001$ and $\Omega = 1,000$ denote a soft inclusion and a stiff inclusion, respectively. In this example, DSIF is computed using the interaction integral method. A detailed implementation of the interaction integral method can be found in [15,38,61]. Moreover, this study's solutions are compared with solutions obtained in [15] using XFEM and in [61] using FEM, and the results will be presented in terms of normalized DSIF, i.e., $\overline{K_I} = K_I/(\sigma_0\sqrt{\pi a})$ where K_I is the mode I DSIF, σ_0 is the magnitude of the applied stress and a is half of the total crack length.

Firstly, we study how the ratio of stiffness, Ω, affects the change of DSIF in time. The radius r and distance d as shown in Fig. 30 are chosen to be 2 mm and 3.6 mm, respectively, which are similar to those introduced in [15]. Fig. 31(a) shows the variations of DSIF at the right crack tip over time for three cases, namely, a plate with soft inclusion, a plate without inclusion, and a plate with stiff

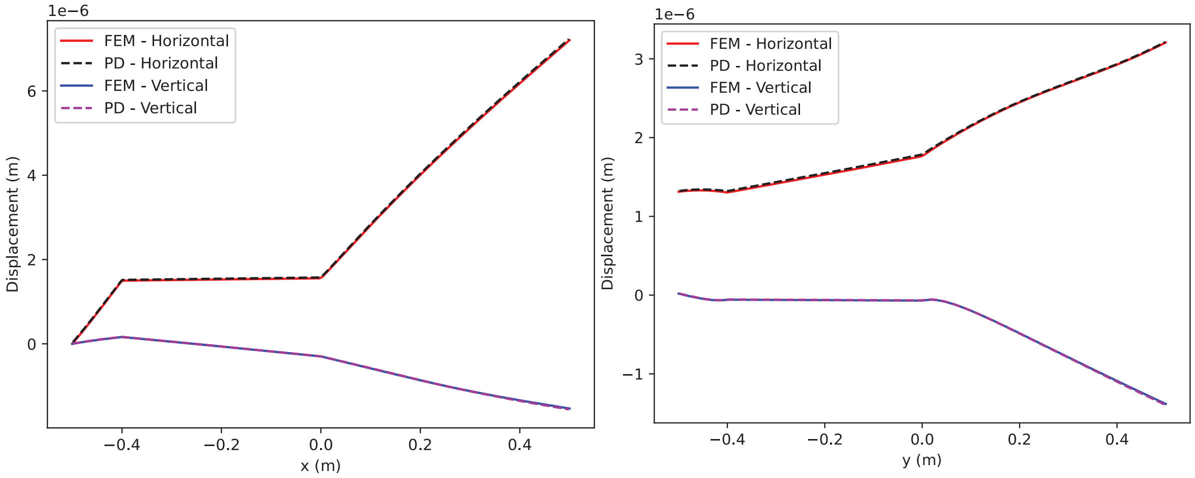

(a) **(b)**

Fig. 25 Variation of displacements **(a)** along $y = -0.2$ m, **(b)** along $x = -0.2$ m in the non-symmetric circular-inclusion plate problem

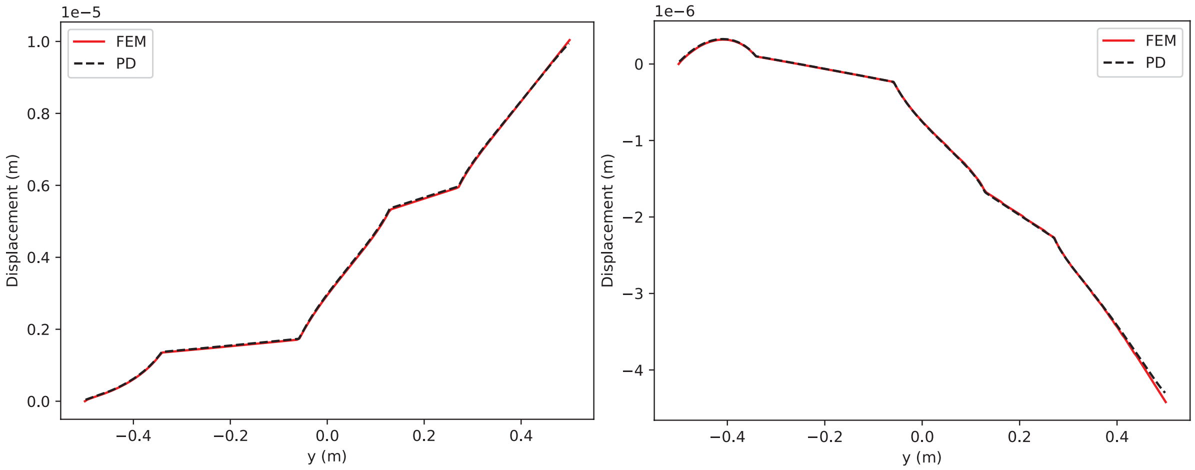

(a) **(b)**

Fig. 26 Displacements along $x = y$ **(a)** Horizontal displacement **(b)** Vertical displacement in the non-symmetric circular-inclusion plate problem

inclusion. The presence of soft inclusion considerably increases the magnitude of DSIF as compared to the case where a plate does not have an inclusion. By contrast, the DSIF sees a decrease in values for a plate with a stiff inclusion. It is noteworthy that the stiffness of inclusion generally does not change the initiation time of the DSIF. Also, the DSIF obtained in PD agrees well with those predicted in [15,61].

Secondly, the influences of inclusion locations are taken into account. Three positions of the inclusion are considered, i.e., $\beta = 0°$, $\beta = 45°$, and $\beta = 90°$. Fig. 31(b) and 31(c) represent the change of DSIF over time with different inclusion locations for a plate with soft inclusion and a plate with stiff inclusion, respectively. For the plate with a soft inclusion, DSIF experiences the highest values in case of $\beta = 45°$ and the lowest values in case of $\beta = 90°$. On the other hand, the DSIF generally has higher magnitude in case of $\beta = 90°$ than other cases for the plate with a stiff inclusion, and the variations of DSIF in other locations are similar to each other. Once again, it can be seen that the solutions obtained by both methods are similar.

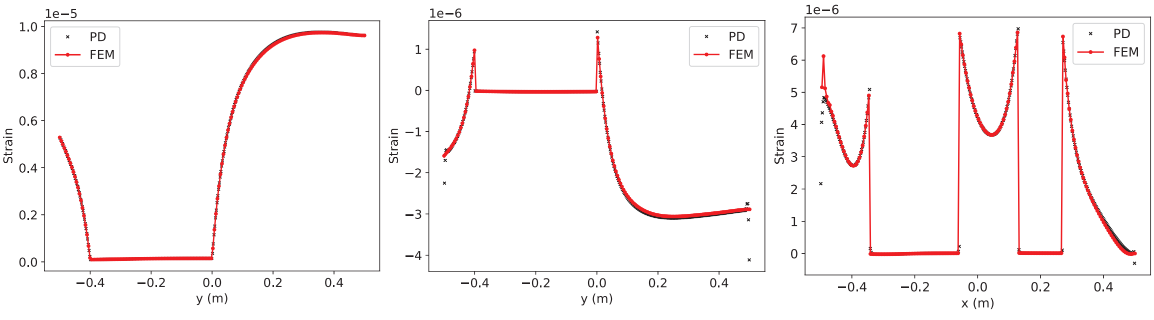

(a) **(b)** **(c)**

Fig. 27 Strain distribution along $x = -0.2$ m **(a)** x-normal strain, **(b)** y-normal strain, **c)** shear strain

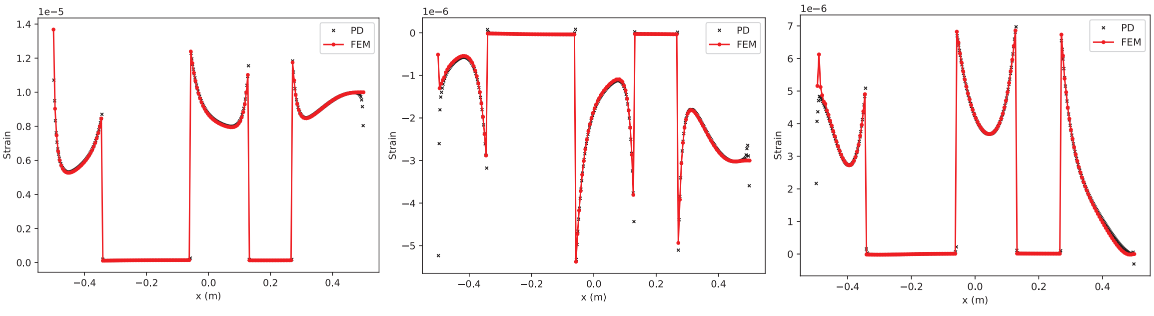

(a) **(b)** **(c)**

Fig. 28 Strain distribution along $x = y$ **(a)** x-normal strain, **(b)** y-normal strain, **(c)** shear strain

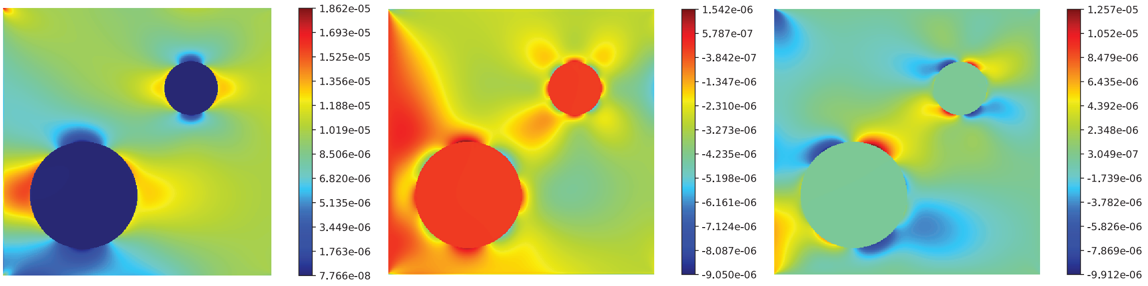

(a) **(b)** **(c)**

Fig. 29 Contours of strain components **(a)** x-normal strain, **(b)** y-normal strain, **(c)** shear strain

5 Conclusions

In the present study, various techniques for interface modeling in OSB-PD are thoroughly investigated. By carrying out numerical experiments, we found that the harmonic average technique yields the best solution as compared to the local solution, i.e., FEM, among four techniques examined in this study. Although there are some differences between PD and FEM in the behaviour near the interface, the overall solutions predicted by both methods are in good agreement with each other. The main advantage of PD is it provides the flexibility in modeling multiple interfaces and cracks without the need to get involved in complicated implementations or time-wasting meshing as in other methods. Defects such as cracks and inclusions can be introduced into a model with ease. Furthermore, the treatment of curve interfaces such as circular inclusions is simple in OSB-PD. The effectiveness of PD in modeling multiple defects are demonstrated through numerous examples including static and dynamics cases,

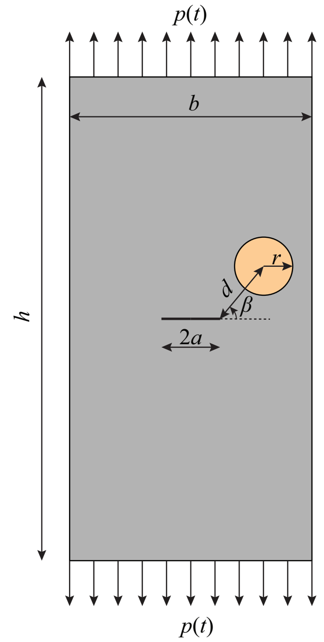

Fig. 30 Geometry and BCs for plate containing a crack and an inclusion

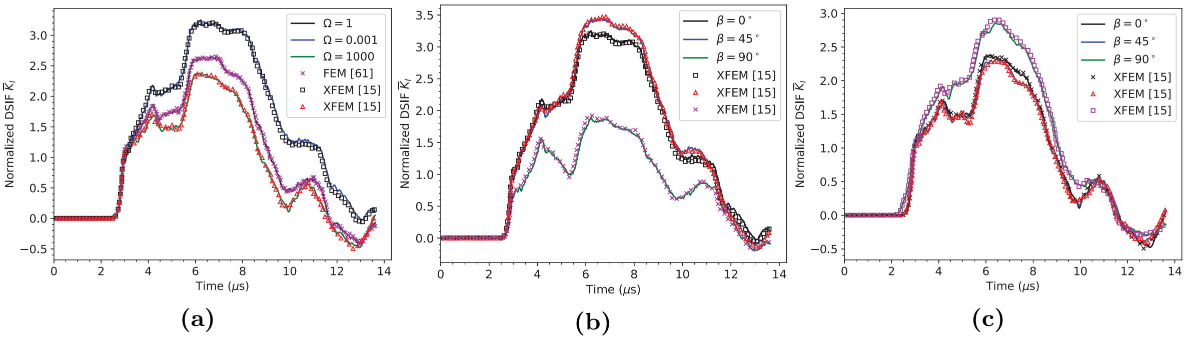

(a) **(b)** **(c)**

Fig. 31 Effect of inclusion stiffness on DSIF at the right crack tip in **(a)**. Effect of inclusion positions on DSIF at the right crack tip for soft inclusion in **(b)** and for stiff inclusion in **(c)**

and they show the great potential of OSB-PD in solving problems with complicated interfaces and defects. Although this study merely focuses on a structure composed of two materials in 2D, it can be easily extended to problems with multiple materials or 3D applications.

Conflict of Interest The authors declare that they have no conflict of interest.

References

1. Biabanaki SOR, Khoei AR, Wriggers P (2014) Polygonal finite element methods for contact-impact problems on non-conformal meshes. Comput Meth Appl Mech Eng 269:198–221
2. Khoei AR, Yasbolaghi R, Biabanaki SOR (2015) A polygonal finite element method for modeling crack propagation with minimum remeshing. Int J Fract 194(2):123–148
3. Huynh HD, Nguyen MN, Cusatis G, Tanaka S, Bui TQ (2019) A polygonal XFEM with new numerical integration for linear elastic fracture mechanics. Eng Fract Mech 213:241–263
4. Chi H, Talischi C, Lopez-Pamies O, H.Paulino G (2015) Polygonal finite elements for finite elasticity. Int J Numer Meth Eng 101(4):305–328

5. Jabareen M (2020) A polygonal finite element formulation for modeling nearly incompressible materials. Meccanica 55(4):701–723
6. Khoei AR, Biabanaki SOR, Yasbolaghi R (2014) A polygonal–FEM technique in modelling arbitrary interfaces on non-conformal meshes: a study on polygonal shape functions. Eur J Comput Mech 23(1–2):15–37
7. Ding S, Shao G, Li A, Su J, Shi H (2017) Numerical simulation of holes and inclusions using adaptive polygonal finite element method. J Mech Sci Technol 31(9):4305–4317
8. Belytschko T, Black T (1999) Elastic crack growth in finite elements with minimal remeshing. Int J Numer Meth Eng 45(5):601–620
9. Sukumar N, Chopp DL, Moës N, Belytschko T (2001) Modeling holes and inclusions by level sets in the extended finite-element method. Comput Meth Appl Mech Eng 190(46):6183–6200
10. Melenk JM, Babuška I (1996) The partition of unity finite element method: Basic theory and applications. Comput Meth Appl Mech Eng 139(1-4):289–314
11. Moës N, Dolbow J, Belytschko T (1999) A finite element method for crack growth without remeshing. Int J Numer Meth Eng 46(1):131–150
12. Sukumar N, Huang ZY, Prévost J-H, Suo Z (2004) Partition of unity enrichment for bimaterial interface cracks. Int J Numer Meth Eng 59(8):1075–1102
13. Areias PMA, Belytschko T (2005) Non-linear analysis of shells with arbitrary evolving cracks using XFEM. Int J Numer Meth Eng 62(3):384–415
14. Bordas S, Moran B (2006) Enriched finite elements and level sets for damage tolerance assessment of complex structures. Eng Fract Mech 73(9):1176–1201
15. Jiang S, Du C, Gu C, Chen X (2014) XFEM analysis of the effects of voids, inclusions and other cracks on the dynamic stress intensity factor of a major crack. Fatig Fract Eng Mater Struct 37(8):866–882
16. Wang Z, Yu T, Bui TQ, Trinh NA, Luong NTH, Duc ND, Doan DH (2016) Numerical modeling of 3-D inclusions and voids by a novel adaptive XFEM. Adv Eng Software 102:105–122
17. Joulaian M, Düster A (2013) Local enrichment of the finite cell method for problems with material interfaces. Comput Mech 52(4):741–762
18. Yu T, Bui TQ, Yin S, Doan DH, Wu CT, Do TV, Tanaka S (2016) On the thermal buckling analysis of functionally graded plates with internal defects using extended isogeometric analysis. Compos Struct 136:684–695
19. Gu J, Yu T, Van Lich L, Nguyen T-T, Tanaka S, Bui TQ (2018) Multi-inclusions modeling by adaptive XIGA based on LR B-splines and multiple level sets. Finite Elem Anal Des 148:48–66
20. Belytschko T, Lu YY, Gu L (1994) Element-free Galerkin methods. Int J Numer Meth Eng 37(2):229–256
21. Cordes LW, Moran B (1996) Treatment of material discontinuity in the element-free Galerkin method. Comput Meth Appl Mech Eng 139(1-4):75–89
22. Krongauz Y, Belytschko T (1998) EFG approximation with discontinuous derivatives. Int J Numer Meth Eng 41(7):1215–1233
23. Wang D, Chen J-S, Sun L (2003) Homogenization of magnetostrictive particle-filled elastomers using an interface-enriched reproducing kernel particle method. Finite Elem Anal Des 39(8):765–782
24. Masuda S, Noguchi H (2006) Analysis of structure with material interface by meshfree method. Comput Model Eng Sci 11(3):131–144
25. Wang D, Sun Y, Li L (2009) A discontinuous Galerkin meshfree modeling of material interface. Comput Model Eng Sci 45(1):57–82
26. Wu CT, Guo Y, Askari E (2013) Numerical modeling of composite solids using an immersed meshfree Galerkin method. Compos B Eng 45(1):1397–1413
27. Belytschko T, Lu YY, Gu L (1995) Crack propagation by element-free Galerkin methods. Eng Fract Mech 51(2):295–315
28. Rabczuk T, Areias PMA, Belytschko T (2007) A meshfree thin shell method for non-linear dynamic fracture. Int J Numer Meth Eng 72(5):524–548
29. Tanaka S, Suzuki H, Sadamoto S, Imachi M, Bui TQ (2015) Analysis of cracked shear deformable plates by an effective meshfree plate formulation. Eng Fract Mech 144:142–157
30. Silling SA (2000) Reformulation of elasticity theory for discontinuities and long-range forces. J Mech Phys Solids 48(1):175–209
31. Silling SA, Epton M, Weckner O, Xu J, Askari E (2007) Peridynamic states and constitutive modeling. J Elast 88(2):151–184
32. Foster JT, Silling SA, Chen WW (2010) Viscoplasticity using peridynamics. Int J Numer Meth Eng 81(10):1242–1258
33. Madenci E, Oterkus S (2016) Ordinary state-based peridynamics for plastic deformation according to von Mises yield criteria with isotropic hardening. J Mech Phys Solids 86:192–219
34. Bang DJ, Madenci E (2017) Peridynamic modeling of hyperelastic membrane deformation. J Eng Mater Technol 139(3):031007
35. Kilic B, Madenci E (2009) Prediction of crack paths in a quenched glass plate by using peridynamic theory. Int J Fract 156(2):165–177
36. Ha YD, Bobaru F (2010) Studies of dynamic crack propagation and crack branching with peridynamics. Int J Fract 162(1):229–244
37. Wang H, Oterkus E, Oterkus S (2018) Predicting fracture evolution during lithiation process using peridynamics. Eng Fract Mech 192:176–191
38. Imachi M, Tanaka S, Bui TQ (2018) Mixed-mode dynamic stress intensity factors evaluation using ordinary state-based peridynamics. Theor Appl Fract Mech 93:97–104
39. Dai M-J, Tanaka S, Bui TQ, Oterkus S, Oterkus E (2021) Fracture parameter analysis of flat shells under out-of-plane loading using ordinary state-based peridynamics. Eng Fract Mech 244:107560

40. O'Grady J, Foster J (2014) Peridynamic beams: A non-ordinary, state-based model. Int J Solids Struct 51(18):3177–3183
41. Nguyen CT, Oterkus S (2019) Peridynamics for the thermomechanical behavior of shell structures. Eng Fract Mech 219:106623
42. Oterkus S, Madenci E, Agwai A (2014) Peridynamic thermal diffusion. J Comput Phys 265:71–96
43. Bobaru F, Duangpanya M (2010) The peridynamic formulation for transient heat conduction. Int J Heat Mass Tranf 53(19-20):4047–4059
44. Javili A, Morasata R, Oterkus E, Oterkus S (2019) Peridynamics review. Math Mech Solids 24(11):3714–3739
45. Madenci E, Oterkus E (2014) Peridynamic theory and its applications. Springer, New York
46. Ren H, Zhuang X, Rabczuk T (2020) A higher order nonlocal operator method for solving partial differential equations. Comput Meth Appl Mech Eng 367:113132
47. Madenci E, Barut A, Futch M (2016) Peridynamic differential operator and its applications. Comput Meth Appl Mech Eng 304:408–451
48. Kilic B, Madenci E (2010) An adaptive dynamic relaxation method for quasi-static simulations using the peridynamic theory. Theor Appl Fract Mech 53(3):194–204
49. Alali B, Gunzburger M (2015) Peridynamics and Material Interfaces. J Elast 120(2):225–248
50. Wang F, Liu L, Liu Q, Zhang Z, Su L, Xue D (2015) Studies of bimaterial interface fracture with peridynamics. In: Proceedings of the 2015 International Power, Electronics and Materials Engineering Conference, Atlantis Press, pp 856–861
51. Ren H, Zhuang X, Rabczuk T (2017) Dual-horizon peridynamics: A stable solution to varying horizons. Comput Meth Appl Mech Eng 318:762–782
52. Zhang H, Qiao P (2018) An extended state-based peridynamic model for damage growth prediction of bimaterial structures under thermomechanical loading. Eng Fract Mech 189:81–97
53. Alebrahim R (2019) Peridynamic modeling of Lamb wave propagation in bimaterial plates. Compos Struct 214:12–22
54. Behera D, Roy P, Madenci E (2021) Peridynamic modeling of bonded-lap joints with viscoelastic adhesives in the presence of finite deformation. Comput Meth Appl Mech Eng 374:113584
55. Xia W, Oterkus E, Oterkus S (2021) Ordinary state-based peridynamic homogenization of periodic micro-structured materials. Theor Appl Fract Mech 113:102960
56. Madenci E, Barut A, Phan N (2018) Peridynamic unit cell homogenization for thermoelastic properties of heterogenous microstructures with defects. Compos Struct 188:104–115
57. Silling SA, Askari E (2005) A meshfree method based on the peridynamic model of solid mechanics. Comput Struct 83(17-18):1526–1535
58. Wang B, Oterkus S, Oterkus E (2020) Determination of horizon size in state-based peridynamics. Continuum Mech Thermodyn
59. Capodaglio G, D'Elia M, Bochev P, Gunzburger M (2020) An energy-based coupling approach to nonlocal interface problems. Comput Fluids 207:104593
60. Madenci E (2017) Peridynamic integrals for strain invariants of homogeneous deformation. J Appl Math Mech Z Angew Math Mech 97(10):1236–1251
61. Song SH, Paulino GH (2006) Dynamic stress intensity factors for homogeneous and smoothly heterogeneous materials using the interaction integral method. Int J Solids Struct 43(16):4830–4866